THE ASTROPHYSICAL JOURNAL, 524:1059–1083, 1999 October 20

H_2 QUADRUPOLE AND H_3^+ EMISSION FROM URANUS: THE URANIAN THERMOSPHERE, IONOSPHERE, AND AURORA

L. M. TRAFTON[1]
McDonald Observatory and Department of Astronomy, University of Texas at Austin, Austin, TX 78712
S. MILLER
Department of Physics and Astronomy, University College London, Gower Street, London WC1E 6BT, England, UK
T. R. GEBALLE[2]
Joint Astronomy Centre, 660 N. A'ohohu Place, Hilo, HI 96720
J. TENNYSON
Department of Physics and Astronomy, University College London, Gower Street, London, WC1E 6BT, England, UK
AND
G. E. BALLESTER
Department of Atmospheric, Oceanic and Space Sciences, University of Michigan, 2455 Hayward Street, Ann Arbor, MI 48109
Received 1999 January 19; accepted 1999 June 5

ABSTRACT

We present an analysis of the near-infrared emission of Uranus, obtained from 1993 to 1995 at the United Kingdom Infrared Telescope (UKIRT) and the NASA Infrared Telescope Facility (IRTF). We report that in contrast to Jupiter and Saturn, prominent emission in the H_2 quadrupole and H_3^+ overtone and fundamental bands occurs globally. The rotational temperature and luminosity of H_2 and H_3^+ were usually found to vary mildly with longitude. The H_2, and possibly the H_3^+, temperature appears to vary with apparition, indicating a long-term variability of Uranus's thermospheric structure. The thermosphere cooled between 1992 and 1995, while the ionosphere either cooled or otherwise suffered a decline in the column of excited H_3^+. The luminosity in $H_2(v = 1)$ was observed as high as 1.6×10^{10} W in 1993 May but remained within 10% of 1.0×10^{10} W for four rotational phases observed in 1995 June near solar minimum. The luminosity in $H_2(v = 0)$ is predicted to be 10–20 times higher and less variable. Similarly, the luminosity in H_3^+ was $\sim 1.1 \times 10^{11}$ W in 1995 June, half the value near solar maximum in 1992 April. The declining temperatures and luminosities may be induced by the declining phase of the solar cycle, when the far-ultraviolet/extreme-ultraviolet flux also declines. Although we have observed evidence of auroral emission by both molecular species, auroral processes apparently play only a secondary role in the observed excitation. The observed H_2 emission is consistent with an H_2 population in the $v = 1$ vibrational state in thermal equilibrium. But H_3^+ appears to deviate significantly from thermal equilibrium in that the $v_2 = 2$ state is underpopulated. The central meridian H_2 intensity distribution is qualitatively consistent with emission from a thick thermosphere. An important result is that the distribution of the H_3^+ fundamental-band emission differs from that of H_2 by having a pronounced concentration toward the subsolar point. We propose that solar extreme-ultraviolet, filtered by Uranus's H corona, is responsible for this concentration and is the dominant source of excited H_3^+ on the planet. The *K*-band spectrum of Uranus's rings indicates a nearly constant, featureless reflectance over this band.

Subject headings: infrared: solar system — planets and satellites: individual (Uranus)

1. INTRODUCTION

The *Voyager* flyby of the outer planets has revealed considerable diversity among their magnetospheres and in how they interact with their ionospheres. This diversity suggests that a comparative planetary study of magnetospheric and ionospheric processes would lead to a more complete understanding of them. Among the outer planets in the post-*Voyager* era, Jupiter has been the main focus of auroral and ionospheric studies. Accordingly, little has since been learned about the ionospheric processes of the other planets. Although Uranus, unlike the other major planets, has only a marginal internal heat source, the *Voyager* Ultraviolet Spectrometer (UVS) has revealed that it is the only major planet with a hot (850 ± 100 K) extended H corona (Herbert et al. 1987; Stevens, Strobel, & Herbert 1993). Uranus's low internal heat source is thought to contribute to the low eddy diffusion coefficient and low homopause, which results in a deep, clear ionosphere. The Uranian magnetosphere is very different from Jupiter's or Saturn's owing both to Uranus's high obliquity and to the planet's tilted and offset magnetic dipole. FUV emission from Jupiter ($\sim 10^{13}$ W) and from other major planets in the Lyman and Werner electronic bands of H_2 has been observed by the *International Ultraviolet Explorer* (*IUE*), *Voyager*, and the *Hubble Space Telescope* (*HST*). However, Uranus's far-ultraviolet (FUV) auroral emission is relatively weak, $(3–8) \times 10^9$ W for wavelengths below Lyα, and is fragmented, unlike on Jupiter (Herbert & Sandel 1994).

The near-IR offers an alternative window that is accessible for ground-based study of planetary auroral and ionospheric phenomena. The atmospheric *K*-band window,

[1] Visiting Astronomer at the Infrared Telescope Facility, which is operated by the University of Hawaii under contract to the National Aeronautics and Space Administration.

[2] Present address: Gemini Observatory, 670 N. A'ohoku Place, Hilo, HI 96720.

which ranges approximately from 1.9 to 2.5 μm, spans several prominent H_2 quadrupole lines and numerous weak lines from the first-overtone band of H_3^+. In addition, the L' band, which is centered at 3.77 μm, spans a number of prominent lines of the H_3^+ fundamental vibrational band. Auroral emission in the quadrupole H_2 lines has been detected for Jupiter (Trafton et al. 1987, 1989a; Kim et al. 1990) but not for Saturn. Trafton et al. (1993) also reported the detection of $S(1)$ H_2 quadrupole line emission from Uranus, emitting 1.2×10^{-17} W m^{-2} in a 3".1 square beam for an intensity of 5.3×10^{-8} W m^{-2} sr^{-1}. The H_3^+ ion is thought to be a major source of protonation for interstellar molecules (Oka 1981; Geballe & Oka 1989; Black et al. 1990), but it was first detected astrophysically on Jupiter (Drossart et al. 1989; Trafton, Lester, & Thompson 1989b; Oka & Geballe 1990). It has also been detected in the ionospheres of Uranus (Trafton et al. 1993) and Saturn (Geballe, Jagod, & Oka 1993). This ion forms when molecular hydrogen, ionized by precipitating charged particles, FUV, or photoelectrons, interacts with H_2. The H_3^+ rotational temperature for Uranus has been determined from the fundamental band: 740 ± 25 K for 1992 April L'-band observations (Trafton et al. 1993) and 669 ± 70 K for 1995 L'-band observations (Lam et al. 1997b). These are close to but less than the 850 ± 100 K temperature of the hot H corona. Finally, Lam et al. (1997b) report that images of Uranus in the light of H_3^+ emission at 3.4–4 μm reveal discernible spatial variation, which may suggest weak auroral activity.

Kim, Fox, & Porter (1992) have considered the distribution of vibrational states of H_3^+ for a photochemical equilibrium model of Jupiter's auroral ionosphere. They show that the observed H_3^+ emission is related to the observed H_2 quadrupole emission owing primarily to reactions between H_2 and H_3^+ in which vibrational energy is exchanged as a consequence of the near-resonance between the $v = (0\text{–}1)$ transition of H_2 and the $v_2 = (0\text{–}2)$ transition of H_3^+. They show that the vibrational distribution of H_3^+ near the altitude peak of Jupiter's emission must deviate from the LTE distribution in the sense that the fractional populations of H_3^+ in the $v = 1$ and 2 vibrational states are less than those of a Boltzmann distribution. Since the behaviors of nonthermal emission from H_2 and H_3^+ are thus connected, we consider both species in this paper rather than in separate papers.

Here we report the detection of nine quadrupole H_2 emission lines in Uranus's thermosphere and the variation of the H_2 rotational temperature with rotational phase during 1993 and 1995. We compare these results with Uranus's H_3^+ emission observed during the same periods. We show that the vibrational population of H_2 is consistent with thermal equilibrium but that this is not the case for H_3^+; this is opposite to what is known about Jupiter's auroral emission. We demonstrate that the H_2 emission and thermosphere extend beyond the limb by $\sim 10\%$ of the radius. Finally, we demonstrate that H_3^+ in the $v_2 = 1$ state is more concentrated toward the subsolar point than is H_2 in the $v = 1$ state and discuss the separate excitation mechanisms for the two species implied by this. A spectrum of Uranus's rings over the K band is also presented.

2. OBSERVATIONS

The observations do not form a homogeneous data set because they were made using two different spectrographs at two observatories over a period when each spectrograph was being upgraded with a larger and more sensitive (and, in one case, larger) array. At the NASA Infrared Telescope Facility (IRTF), we used the CSHELL long-slit echelle spectrograph at resolving powers of 10,000–20,000 during 1993–1994 to observe individual H_2 quadrupole emission lines in the K band and the relatively bright H_3^+ $\nu_2(4, 3, -1 \rightarrow 3, 3)$ line at 3.534 μm. At the United Kingdom Infrared Telescope (UKIRT), we used the long-slit spectrograph CGS4 at resolving powers of 300–1500 during 1993–1995. To observe all latitudes as the planet rotated, we oriented the spectrographic slit along the planet's central meridian (CM) for all CSHELL spectra and also for our 1995 CGS4 spectra. The earlier CGS4 spectra, which were obtained with a wider slit, were obtained with the slit at a position angle of 0°. Tables 1 and 2 provide logs of the observations and further details are provided in Appendix A. Some of the 1995 observations in the L' band have been previously reported by Lam et al. (1997b).

Along with the brightest line of the 3.534 μm manifold of the H_3^+ fundamental, only the $S(1)$ and $Q(1)$ H_2 quadrupole lines were detected with an adequate signal-to-noise ratio (S/N) using CSHELL owing to problems in cancelling its circular variable filter (CVF) fringing. For CGS4, nine H_2 lines and numerous lines of the H_3^+ fundamental band were detected. Although the weak overtone bands of H_3^+ were

TABLE 1

IRTF OBSERVATIONS

Date [a] (UT)	Lines [b]	Mid-Observation[a] (UT)	Exposure (hr:minute)	Air Mass[c]	Pixel Size[d] (arcsec)	Relative Phase[e]	Resolution	Comments
1993 May 25...	$S(1)$	13:32	0:20	1.35	0.28 × 1	0	21500	Clear
1993 May 25...	$S(1)$	14:16	1:00	1.35	0.28 × 1	0.04	21500	Thin cirrus
1993 May 26...	$Q(1)$	14:09	0:48	1.34	0.28 × 1	0.43	21500	~1"; clear
1993 May 27...	$S(1)$	11:59	0:47	1.46	0.28 × 1.5	0.70	13300	"Good"; clear
1994 Aug 21 ...	3.534 μm H_3^+	08:42	0:50	1.36	0.20 × 1.5	0	13300	~1".1; clear
	3.534 μm H_3^+	10:58	0:30	1.92	0.20 × 1.5	0.13	13300	~1".1; clear
1994 Aug 22 ...	3.534 μm H_3^+	10:38	0:10	2.1	0.20 × 2	0.50	10800	~1".3 clear; occasional thin cirrus

[a] Dates and times are given as Universal Time
[b] Fundamental band of H_2 or H_3^+
[c] Averaged over each observation
[d] With smaller dimension along the slit, which is oriented along the planet's CM; Larger dimension is slit width
[e] Rotational phase normalized to unity, relative to the first observation listed for each year

TABLE 2

UKIRT OBSERVATIONS

Date[a] (UT)	Mid-Observation[a] (UT)	Exposure (hr:minute)	λ Range[b] (band or μm)	Air Mass[c]	Pixel Size[d] (arcsec)	Relative phase[e]	$\lambda/\delta\lambda$	Comments
1993 May 3.....	14:14	0:20	K band; rings	1.40	3.08 × 3.08	...	340	Clear; calibration
.....	15:19	0:29	4 μm	1.35	3.08 × 3.08	0	1200	Clear
1993 May 4.....	12:57	0:39	S(1,2) and R(6)	1.90	3.08 × 3.08	0	1300	0.″7; clear
.....	14:09	0:22	4 μm	1.35	3.08 × 3.08	0.324	1200	0.″7; clear
.....	15:13	0:16	Q(1–3)	1.35	3.08 × 3.08	0.138	700	0.″7; clear
1993 May 5.....	12:54	0:24	4 μm	1.62	3.08 × 3.08	0.644	1200	Clear
.....	14:04	0:24	S(1,2)	1.45	3.08 × 3.08	0.462	1300	Clear
.....	15:06	0:24	Q(1–3)	1.35	3.08 × 3.08	0.524	700	Clear
1994 Jul 20	11:08	2:24	4 μm	1.50	1.54 × 4.62	0	1200	Clear
1994 Jul 23	12:30	0:40	4 μm	1.8	1.54 × 4.62	0.256	1200	Thin patchy clouds
1995 Jun 11.....	14:43	0:44	2.28 μm	1.45	1.23 × 1.35	0.162	900	0.″8; clear
1995 Jun 12.....	11:45	0:44	2.28 μm	1.46	1.23 × 1.35	0.382	900	1.″2; occasional cirrus
1995 Jun 13.....	11:31	0:48	2.28 μm	1.50	1.23 × 1.35	0.761	900	1+″; occasional thin cirrus
1995 Jun 14.....	11:07	0:32	2.28 μm	1.53	1.23 × 1.35	0.130	900	<1″; clear
1995 Jun 11.....	11:55	0:54	3.77 μm	1.43	1.23 × 1.35	0	1500	0.″8; clear
1995 Jun 12.....	13:27	0:57	3.77 μm	1.60	1.23 × 1.35	0.480	1500	1.″2; occasional cirrus
1995 Jun 13.....	13:15	1:18	3.77 μm	1.40	1.23 × 1.35	0.861	1500	~1+″; occasional thin cirrus
1995 Jun 14.....	12:11	0:30	3.77 μm	1.36	1.23 × 1.35	0.186	1500	~1″; clear

[a] Dates and times are given as Universal Time.
[b] Or wavelength at midspectrum for broadband spectra.
[c] Averaged over each observation.
[d] With smaller dimension along the slit, which is oriented along the planet's CM; the larger dimension is slit width.
[e] Rotational phase normalized to unity, relative to the first observation listed for each year for each species.

also detected with CGS4, their S/N was too low for analyses other than deriving the vibrational temperature of H_3^+. The analysis of these lines is described below.

3. REDUCTIONS

3.1. *Procedure*

The IRTF and UKIRT observations were reduced following standard procedures, using the IRAF spectral image-processing package, to flat-field, dark-subtract, detilt (required for some CGS4 spectra), and wavelength-calibrate (using Ar, Ne, or Xe spectra of arc lamps; for CSHELL, which has a narrow bandpass, these spectra were obtained in various orders). The elimination of the fringing and vignetting was only partially successful for CSHELL owing to its irreproducible CVF settings at different wavelengths. Successive co-added pairs of spectra were differenced to provide both object-sky and sky-object spectra. Because of the possible contamination by clouds or other problems, these individual difference frames of data were examined and rejected if they deviated excessively from the norm. Flux calibration was achieved using observations of bright stars; details are provided in Appendix B.

In order to study the emission lines of H_2 and H_3^+ more easily, the fully reduced spectra are presented with the underlying "continuum" spectrum subtracted. Details of this procedure are found in Appendix C. This appendix also contains a discussion of possible contamination of the emission lines by narrow absorption lines of H_2 and CH_4 and a caveat in the correction for telluric absorption lines. With few exceptions we consider these effects to be unimportant in our data.

Uranus's K-band spectrum, averaged over the three brightest rows of the array and averaged over the nights of 1995 June 11–14, is shown in Figure 1. Nine H_2 lines from the $v = 1$ level are detected along with a few weak emission lines of the first-overtone band of H_3^+ [most notably R(6) at 2.093 μm]. Figure 2 shows the same spectrum but with the underlying "continuum" spectrum removed and all rows of the image averaged before normalizing to the three brightest rows to permit extracting the emitting H_2 column. The H_2 line intensities in the K band spectra were used to obtain the rotational temperature of the H_2, as described in § 4. We focused our H_2 analysis on the stronger emission lines, i.e., S(1), S(2), S(3), Q(1), Q(2), and Q(3), because the relative error

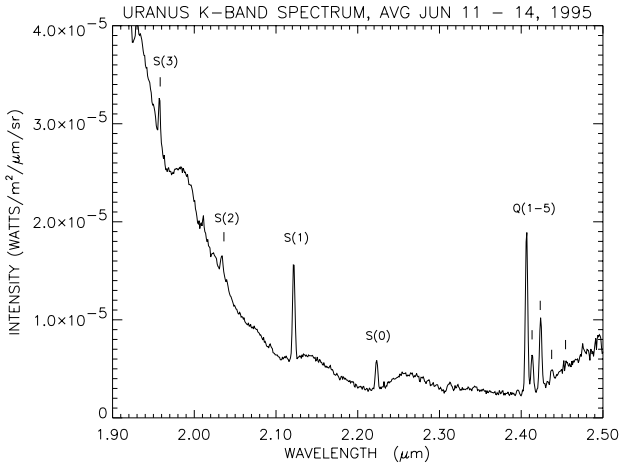

FIG. 1.—Observed spectrum of Uranus's K band averaged for the nights of 1995 June 11–14, taken with the CGS4 spectrograph at the UKIRT. The brightest three rows of the spectral image, which would span Uranus's undistorted 3.″7 central meridian, have been averaged. The H_2 quadrupole emission lines are prominent, especially the Q branch. Weak emission features from the overtone band of H_3^+ are also visible. The emission spectrum is superimposed on broad absorption bands because of the pressure-induced dipole of H_2. The dipole spectrum of CH_4 also contributes to the background absorption near S(0) and the Q branch. The spectral structure near 2.01 μm and longward of 2.45 μm is believed to be caused by incomplete cancellation of telluric features and therefore spurious.

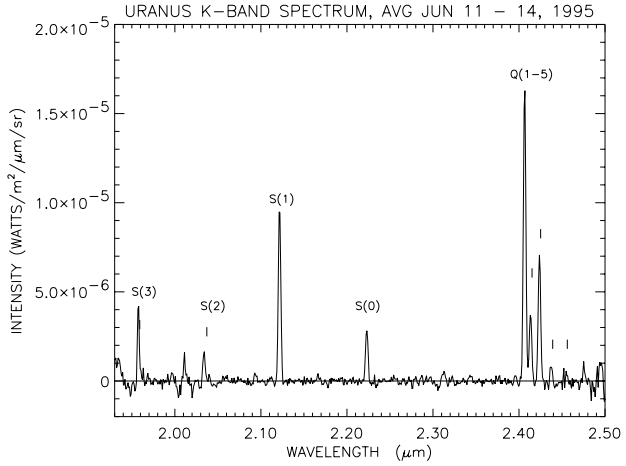

FIG. 2.—Uranus's continuum-subtracted H_2 quadrupole emission spectrum shown for the nightly average of the 1995 June observing run. The lines are indicated for the fundamental H_2 band.

in their derived fluxes due to noise and to background CH_4 absorption is smaller. The L'-band spectra of Uranus, containing manifolds of H_3^+ lines from the $v_2 = 1$ level, were analyzed (assuming they arise in a single, isothermal, ionospheric layer well above the homopause) to determine the rotational temperature of the H_3^+. The vibrational temperature of the H_3^+ was derived from comparison of the unblended $R(6)$ overtone line at 2.093 μm to the partially blended $Q(3)$ fundamental subband at 3.986 μm. The blending of $Q(3,0-)$ with the weaker $Q(3,1-)$ line was accounted for. The rotational and vibrational H_3^+ temperatures are discussed in § 5.

The spatial profiles of H_3^+ and H_2 also were examined to determine their CM distributions of these molecules in their first excited vibrational states. Here we included re-reduced H_3^+ data from 1995 June, the spectra of which were published by Lam et al. (1997b). Figure 3 shows the re-reduced spectrum averaged over the 1995 June observing run for the short wavelength portion of the L' band.

The four consecutive nights of observations obtained in 1995 are of special importance because they form the basis of our study of the variations in Uranus's emission spectrum with rotational phase. Because of the smaller slit width used in 1995 to match the smaller diode size of the new SBRC detector array, some of the light from the standard stars was lost on its jaws, so the throughput was dependent on the seeing (92%–75% for seeing 0.″9–1.″4) as well as on the sky extinction. Consequently, special care was taken to ensure that the relative flux calibration was accurate enough to reveal the nightly differences. The absolute intensity was derived in two stages using a primary and secondary standard star, and the nightly spectra were scaled to give a constant K-band continuum intensity before subtraction of the continuum. The details are given in Appendix D. The resulting absolute intensity calibration was applied to the K-band spectrum of Uranus surveyed in Figure 1, which is the basis of the scales of Figure 2 and the nightly 1995 H_2 emission spectra.

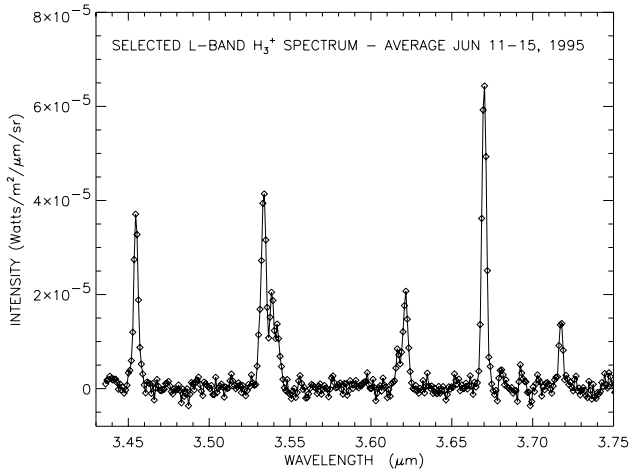

FIG. 3.—Spectrum of Uranus's H_3^+ manifolds obtained with CGS4 during 1995 June, used for our study of the H_3^+ intensity variation along the central meridian (see Table 8).

3.2. *Central Meridian Profiles*

For characterization and study of the global excitation, the latitudinal distribution of the emission intensity along Uranus's central meridian was modeled for H_3^+ and H_2. The observed CM emission profiles are compared in § 7. These were obtained by integrating each spectral feature over wavelength for each continuum-subtracted row of the array lying along the slit. The CM continuum profile is not useful for locating the planetary limbs or modeling the limb darkening because it is distorted by the diffuse reflection of sunlight from the planet's projected rings, which approach closest to the disk at the CM limbs. The distortion is evident in Figure 4, which compares the continuum and emission profiles along the CM and shows that the continuum has a much greater FWHM. The concave appearance of the continuum profile at the longer wavelength is due mostly to the brighter rings rather than to planetary limb brightening in the continuum, which exists as a result of the pressure-induced absorption of H_2 and stratospheric haze. Because of the uncertainty in the ring albedo and geometry, the

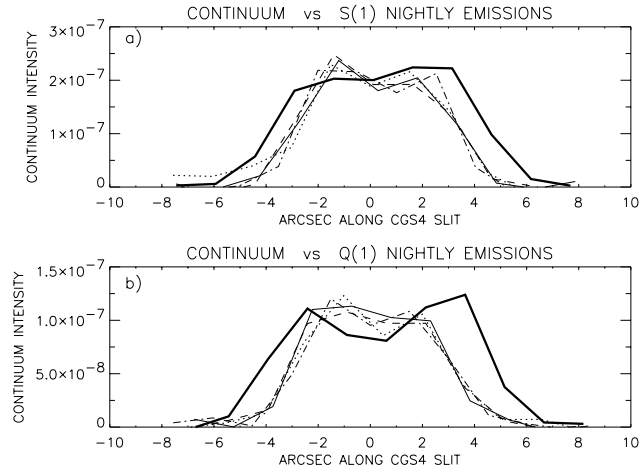

FIG. 4.—Distribution of Uranus's continuum intensity along the central meridian (*heavy line*) adjacent to prominent H_2 quadrupole lines compared with the wavelength-integrated intensities of those H_2 lines for each of four nights in 1995 June. The H_2 profiles have been scaled to the continuum intensity for comparison. The June 11–14 H_2 profiles are shown with the light solid, dotted, dashed, and dot-dashed lines, respectively. The comparison is shown for (*a*) the $S(1)$ line and (*b*) the $Q(1)$ line. The continuum profile is wider because it includes sunlight reflected by Uranus's unresolved rings.

contribution of the rings to the continuum profile was not removed.

Figure 4 also shows that instead of being centered relative to the H_2 emission, the continuum is shifted in the direction toward the visible (south IAU) pole, which is to the right of center on the plot. N.B.: For all of the CM profiles shown in this paper, Uranian north (IAU) and the visible equator are to the left and the visible south pole is to the right of center. This asymmetry persisted over at least four nights during which the precession of the rings was less than 6°. The offset continuum likely arises from the orbital asymmetry of the rings (see Baines et al. 1998). Tropospheric polar haze is unlikely to contribute to this apparent offset because of the low planetary albedo and the large width of the continuum profile. We have no evidence that the emission profile is not centered on the planet itself.

Plots of the CM variation of the H_2 quadrupole $S(1)$ and $Q(1)$ line emission for the successful CSHELL observations obtained in late May of 1993 are shown in Figure 5. Note the clear bimodality of the profiles, especially for the $Q(1)$ line (*solid line*). Bimodality is also apparent to various degrees in the three $S(1)$ profiles, which sample different CM longitudes. The lower spatial resolution CGS4 emission profiles plotted in Figure 4 confirm the bimodality.

Three independent CSHELL observations of the brightest line of the fundamental-band H_3^+ complex at 3.534 μm were made on 1994 August 21 and 22. Figure 6 shows the extent of the agreement of the CM intensity derived from these spectral images, which provides an indication of the uncertainty in the shape and strength of these CM profiles. With only 0.″20 square diodes in 1994 and the failure of every fourth row of the detector array, these CSHELL data appear noisy. However, all three profiles have only a single peak instead of being bimodal as for H_2, suggesting that the H_3^+ emission is brightest near the sub-Earth latitude, unlike the case for H_2. Two of the three profiles agree, but the third (*dashed line*; August 21 at 10:58 UT) appears to show significantly elevated emission near the center of the disk. Their FWHMs vary between 3.″8 and 4.″7, with the smallest FWHM corresponding to the most peaked profile, suggesting a localized enhancement.

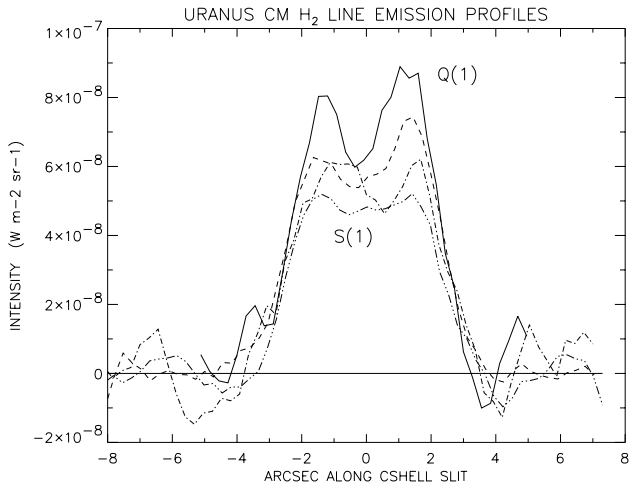

FIG. 5.—Observed CSHELL spatial profiles of the quadrupole H_2 emission for the $Q(1)$ line (*solid line*) and three observations of the $S(1)$ line showing the distribution of integrated line emission along Uranus's central meridian during late May of 1993. To facilitate comparison, the profiles have been aligned along the slit and boxcar smoothed over three diodes.

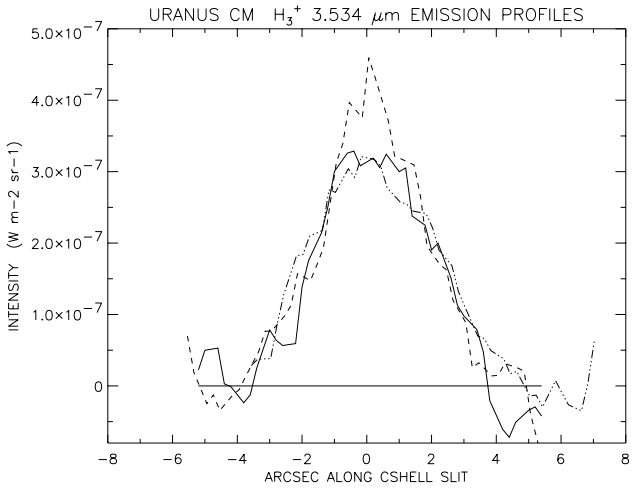

FIG. 6.—Three independent CSHELL profiles of the brightest line of the 3.5337 μm manifold of H_3^+ distributed along Uranus's central meridian during 1994 August. Each profile has been boxcar smoothed over three 0.″2 diodes. Note the pronounced difference in the central meridian distribution from that of H_2 shown in Fig. 5. The logged estimated seeing varies from 1.″2 to 1.″4. The profiles shown by the solid and dashed lines were taken on August 21 and that shown by the triple-dot-dashed line was taken on August 22. Note the elevated peak of the profile shown by the dashed line, a potential auroral enhancement.

3.3. *Ring Spectrum*

The spectrum of Uranus taken on 1993 May 3 with the 75 line mm^{-1} grating spanned the K band, with the slit approximately parallel to the planet's equator. Ring 6 through the ϵ ring lie about 2.″9–3.″6 from the planet's center (Baines et al. 1998). The rings are therefore resolved in the 3.″1 rows of the array straddling the row centered on the planet. These rows, however, include some contribution of the planet. Owing to a small offset of the central row from the center of the planet, the contamination of the ring south of the planet was relatively small. We were able to remove the planet's contribution by subtracting the central row from the southern row after scaling ($\times 0.12$) the central row to null out the H_2 emission lines in the difference spectrum. This K-band ring spectrum is plotted in Figure 7 as projected reflectivity, I/F, averaged over the diode area versus the wavelength; however, the ring particle reflectivity is much larger owing to the relatively small projected area of the particles (Baines et al. 1998). The ring brightness also varies with azimuth. Within the statistical uncertainty, the reflectivity appears to be constant with wavelength, as suggested by the J-, H-, H'-, and K-band images of Baines et al. (1998). No spectral features are detected. We did not detect the rings in our L'-band spectral images.

The rings do not affect the emission profiles because (1) the continuum spectrum was completely removed in deriving the emission spectrum for each detector row along the slit and (2) the diffuse reflection of the planet's emission spectrum by the rings is negligible relative to the planet's emission owing to the low ring reflectivity (see Fig. 7).

4. THE H_2-QUADRUPOLE EMISSION SPECTRUM

In modeling the spectrum of the H_2 quadrupole line emission, we assumed that the global-scale emission is nonauroral because *Voyager* UVS data indicate that the auroral emission is highly localized, being fragmented along a periodically visible auroral arc (Herbert et al. 1987).

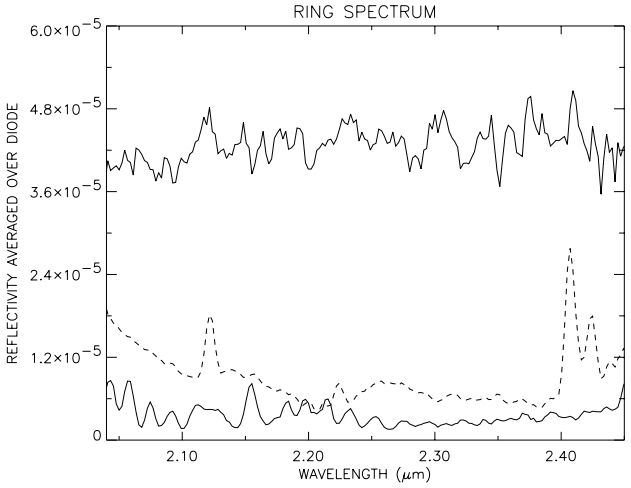

FIG. 7.—*K*-band spectrum of Uranus's rings south of the planet on 1993 May 3 (ring 6 through the ϵ ring). The extracted ring spectrum is shown at the top, and the error spectrum is shown near the bottom. The dashed spectrum is Uranus's central meridian spectrum scaled to cancel the H_2 emission spectrum after subtraction from the ring spectrum, which was contaminated by Uranus's spectrum, to produce the spectrum shown at the top. These spectra are all smoothed over three diodes. The albedo is nearly constant across the *K* band, and no statistically significant spectral features are evident. The reflectivity is averaged over the diode area; the actual ring reflectivity is much higher owing to the small ring area.

Hence, the observed global H_2 emission is assumed to arise entirely from the hot thermosphere via spontaneous decay of vibrationally excited rotational levels to the ground state. We also assumed that H_2 is normally in vibrational as well as rotational thermal equilibrium. This allows us to relate the total H_2 column to the column of excited and emitting H_2. We confirm a posteriori that in contrast to the nonequilibrium population of Jupiter's H_2 vibrational levels due to the auroral cascade of charged particles (Cravens 1987; Kim et al. 1990), we do not need an excess of $H_2(v = 1)$ over what might be expected thermally in order to account for our results. We further assumed that the emission is not attenuated by hydrocarbon absorption, which we also confirm a posteriori. Other possible sources of absorption were neglected. Accordingly, we modeled the emission as arising from a globally uniform, vertically inhomogeneous, elevated thick shell enveloping the planet. This shell, however, is isotropically emitting, nonscattering, and optically thin. Even in cases where we may have also observed auroral emission, this underlying thermospheric emission should be present.

4.1. *The Effective Uranian Air Mass and Mean Disk Intensity*

Nightly rotational temperatures and columns for H_2 were determined from observations of Uranus's H_2 emission obtained during 1993 and 1995. For the 1993 observations, only the continuum-subtracted emission spectrum from the brightest row of the array, approximately centered on Uranus, was modeled because this row sampled a 3.″08 square pixel, 87% of the area of Uranus's disk. Model simulations indicate that the observed intensity is very insensitive to the seeing for this pixel size and location, dropping 12% as the seeing rises from 0″ to 3″. (Somewhat greater variations come if the pixel is off-center, owing to the limb-brightened emission.) So the observed seeing-smeared emission intensity is a suitable approximation to the actual mean intensity averaged over this pixel. However, the effective Uranian air mass, or secant through the planet's atmosphere, depends on the seeing as well as the geometry. For our shell model with the 3.″08 square diodes, the lower limit on the air mass is given by perfect seeing and is 1.32. The upper limit is given by bad seeing where light is redistributed over the slit and is 2.09. We adopt an average Uranian air mass of 1.7 for the 1993 spectra for the purpose of converting the observed emission intensity to the corresponding vertical intensity for constraining the H_2 column in the top layer.

For the 1995 observations, each continuum-subtracted spectrum was summed over eight rows (9.″8) centered on the planet to ensure including all the emission entering the slit, because this was the procedure used to correct the distortion of the spectral intensity by the nightly variable seeing. The resulting spectra were then renormalized ($\times 1.862$) to agree with the emission spectrum averaged over the four nights for just the three brightest rows, corresponding to the mean disk emission intensity through the 1993 calibration. The effective pixel size for the mean intensity was thus 3.″69 $\times$ 1.″35, or almost half of the disk area. The effective Uranian air mass is nearly the same as for the average over the slit done for perfect seeing, namely, 2.07 for our model (moderate seeing merely redistributes the light over the slit). This is compared to the value 1.57 for a thin emitting shell.

4.2. *Modeling the Spectrum*

The emitting H_2 layer of the atmosphere is not isothermal because *Voyager* UVS observations (Broadfoot et al. 1986) indicate that Uranus's $T(P)$ structure rises above the stratosphere to the asymptotically high values observed in the exosphere and corona. To account for the cooler layers, our model assumes the *Voyager*-determined $T(P)$ structure below an adjustable, hot, isothermal, top layer. Most of the emission originates in this top layer, the temperature and H_2 column of which we adjust to fit the observed spectra. For the $T(P)$ structure below the top layer, we adopted Herbert et al.'s (1987) cooler model, which is based on the solar rather than the stellar occultation. This, rather than the hotter, model was adopted in order to concentrate the emission at higher, hotter altitudes where the isothermal approximation has more validity. Although the *Voyager* results indicate that Uranus's upper thermosphere actually has a temperature gradient, the isothermal approximation yields a pretty good fit to our H_2 data and allows us to make an in-kind comparison with Jupiter's published rotational temperatures.

We constructed a synthetic emission spectrum for the H_2 quadrupole line emission using the Einstein coefficients of Turner et al. (1977) and wavelengths generated from the energy levels given by Dabrowsky (1984) and by Jennings & Brault (1983) for the excited ro-vibrational levels of the ground electronic state. The formulation for the emission strengths followed that of Cravens (1987) and Kim et al. (1990), except that the rotational partition function was determined by a direct summation over the rotational states in the $v = 1$ vibrational level rather than by the approximation neglecting nuclear spins used by the latter.

A singlet Ar line in the hollow cathode spectrum (at 2.3973 μm), taken on June 14 using the same instrumental setup and normalized to unit area, served as the modeled H_2 emission profile. At the resolution used, the intrinsic widths of the Ar and H_2 lines are negligible compared to

TABLE 3

MODEL URANUS ATMOSPHERE FOR 1995 JUNE

Temperature [a] (K)	H_2 Pressure [a] (μbar)	Layer Temperature [b] (K)	Layer H_2 Column [c] (cm amagat)
624	0.159	624	1.76
500	0.161	562	0.0182
500	0.198	500	0.409
200	0.997	350	8.83
150	9.97	175	99.0
72	847	111	9000

[a] At lower boundary of layer; except for top layer, values are from Cool *Voyager* model of Herbert et al. 1987.

[b] Average of layer boundary values; the 4th and 5th layers down would be 130 K hotter in the Hot *Voyager* model. The temperature of the top layer is derived in this paper.

[c] Total H_2 column for each layer assuming Boltzmann population of the vibrational levels at the layer temperature; note that the second layer is very thin in order to allow a rapid transition in temperature from the top isothermal layer to the *Voyager* structure. The column of the top layer is derived in this paper.

this instrumental line-spread function (LSF). For the 1993 spectra, taken with the 150 line mm^{-1} grating, the S branch was observed in second order and the Q branch was observed in first order. We scaled the width of this 1995 Ar line profile so that the convolved synthetic spectrum fitted the observed 1993 spectra. The fitted width remained unchanged for the Q branch but was effectively halved for the S branch.

To approximate the variation of temperature with pressure between the tropopause and the homopause (~ 1 μbar), the emitting shell was modeled by a series of six concentric isothermal shells above the 1 mbar level. Table 3 lists the temperature and pressure at the modeled shell boundaries and the temperature and H_2 column for each isothermal shell for the particular case of our averaged 1995 June observations. Owing to the sharp drop in temperature below the homopause, only the top (hottest) three-four layers were found actually to contribute to the observed emission. For the averaged 1995 observations, layers below the third contribute only 0.4% to the observed $Q(1)$ emission. As intended, most of the emission (91%–97%) originates in the extended top isothermal layer, above the 0.04–0.31 μbar level.

In order to preserve the total H_2 column while fitting, it was necessary to adjust the H_2 columns of the top three or four layers, each assumed to be in thermal equilibrium, in response to adjustments to the temperature of the top layer. This was done consistently with the *Voyager* $T(P)$ structure below the top layer; e.g., making the top layer thicker comes at the expense of thinner lower layers having lower mean temperatures. The second layer is very thin in order to accommodate a rapid drop in temperature from the high value fitted in the extended isothermal top layer to the 500 K value consistent with the *Voyager* $T(P)$ distribution (Table 3). By design, this layer contributes a negligible amount to the observed emission. The third layer is 500 K throughout and was adjusted mostly to compensate column changes in the top layer during the fitting. It contributes 2.5%–5% to the average 1995 emergent $Q(1)$ emission. The fourth layer spans the transition from 500 to 200 K. Its only adjustment occurred for 1995 June 12, when the thermosphere was the coolest: its topmost pressure level was lowered. The temperatures of the fourth and fifth layers distinguishes which of Herbert's (1987) models is employed. If Herbert et al.'s hot model were chosen (from the stellar occultations), these layers would be about 130 K hotter and the emergent $Q(1)$ emission from the fourth layer would rise from 0.4% to about 28% of the total emission in the case of our averaged 1995 data.

4.3. *The Derived Temperatures*

The H_2 rotational temperature was determined mostly by fitting the nearby three brightest lines of the Q branch ($J = 1$–3) in order to avoid wavelength-dependent variations in the instrumental LSF and planetary absorptions. The fitting of the synthetic spectrum was done by varying the temperature of the top layer and the other free parameters mentioned above to minimize χ^2 over 19 channels spanning these Q branch lines. An rms average of the same number of channels was measured for a well-behaved region of the background baseline spectrum at wavelengths just short of the Q branch. This formed the empirical noise comparison for calculating the χ^2 of the fit (17 degrees of freedom). The fits were done for those 1993 observations that included the Q branch and for each nightly spectrum of the 1995 run and their average spectrum. For the 1993 observations, we simply used the $T(P)$ structure below the top layer from the average 1995 model. The emitting species proved to be hotter in 1993, and so the observed emission was relatively less sensitive to the temperature structure of these lower layers (Table 4).

Figure 8 shows the optimal fit to the Q branch of the average 1995 spectra and the rms fit residual. The fit is typical of those to the nightly spectra except that the latter have greater noise and residuals. The same fitted spectrum extended to cover all the H_2 emission lines in the K-band is superposed on the observed spectrum shown in Figure 9 in

TABLE 4

1993 ROTATIONAL TEMPERATURES OF H_2

Source	May 4 (K)	May 5 (K)
From Q branch	675	788
1 σ	656–698	761–816
From $S(2)$ vs. $S(1)$.....	940	738
1 σ	871–1032	636–865

TABLE 5

1995 ROTATIONAL TEMPERATURES FOR H_2

Date (UT)	T_{rot} [a] (K)	68% Confidence Interval[b] (K)	90% Confidence Interval (K)	H_2 Column[c] (cm amagat)
1995 Jun 11	640	(621–660)	(610–670)	1.39
1995 Jun 12	591	(568–613)	(555–629)	2.78
1995 Jun 13	622	(594–621)	(600–645)	1.97
1995 Jun 14	643	(621–666)	(609–680)	1.28
1995 Average.....	624	(615–634)	(609–641)	1.76

[a] From Q-branch emission; the rms of the average (624 ± 24 K) is slightly higher dispersion than the average 68% confidence interval of ±20 K.

[b] Approximately ±1 σ range.

[c] Total H_2 column for the top isothermal emitting layer.

order to assess the quality of the fit for the S branch and the weaker lines of the Q branch and to verify our modeling assumptions. The poor fit at $S(3)$ is due to the incomplete cancellation of a strong telluric CO_2 band blending this line. The derived rotational temperature for the average of all Uranus H_2 emission spectra observed during 1995 June is $T = 624$ K, with a 90% confidence interval of 609–641 K (Table 5). The confidence limits neglect the uncertainty of the contribution to the emission from the discrete *Voyager*-constrained underlying layers. The corresponding column of hot equilibrium H_2 in the top layer is 1.76 cm amagat.

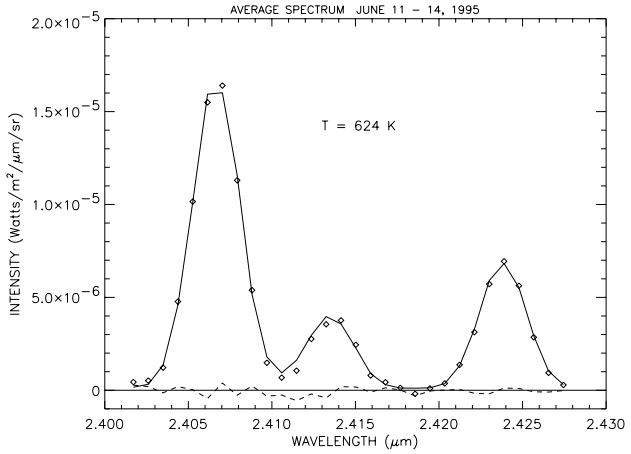

FIG. 8.—Comparison of Uranus's H_2 Q-branch emission spectrum averaged over several planetary longitudes during 1995 June 11–14, with the synthetic emission spectrum fitted to determine the H_2 rotational temperature. From left to right, the lines are $Q(1)$, $Q(2)$, and $Q(3)$. The residual of the rms fit is shown by the dashed line.

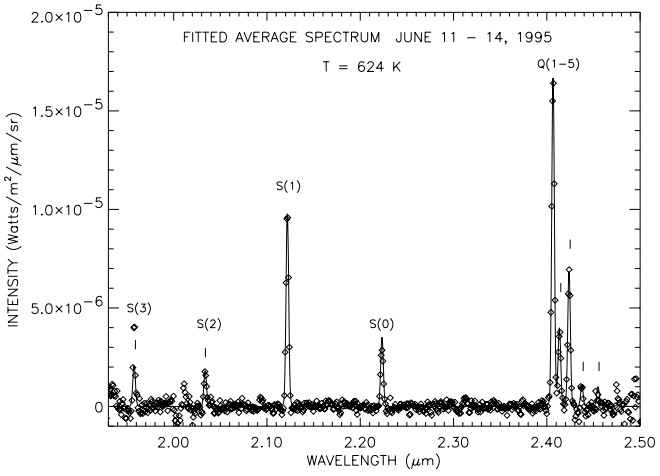

FIG. 9.—Favorable comparison of Uranus's K-band H_2 emission spectrum with the synthetic H_2 spectrum fitted to just the Q branch as shown in Fig. 8 and extended to cover the K band. The diamonds represent the observations, and the solid line is the fitted synthetic spectrum for 1.76 cm amagat H_2 at rotational temperature 624 K in the top, hot, layer.

Figure 10 shows the $S(2)$ and $S(1)$ lines of the S branch for 1993 May 4, when the thermosphere was the hottest we observed. The resolution and dispersion were higher for the 1993 S-branch spectra owing to the use of the 150 line mm^{-1} grating in the second order instead of the 75 line mm^{-1} grating in the first order used for the 1995 spectra. The greater relative strength of the weak $S(2)$ line in the 1993 spectrum than in 1995 is evident and indicates that the rotational temperature was significantly higher than in 1995. Modeling this S-branch spectrum in the same manner as for the Q branch yields a temperature of 940 (+92, −69) K. The derived temperatures for the nightly 1993 S-branch observations agree with our independent analysis based on the measured ratio of the equivalent widths of the $S(2)$ and $S(1)$ lines and the resulting ratio of the line strengths. Both the S -ranch and Q-branch analyses support higher temperatures in 1993. Since the time it takes for the planet to rotate one slit-width (1.8 hr) is less than the time between the S- and Q-branch observations (Table 2), the different temperatures correspond to different longitudes on the planet. This difference could occur if the elevated S-branch emission were auroral.

The rotational and vibrational temperatures of H_3^+ are listed in Table 6. Our assumption that the H_3^+ emission arises from an isothermal, ionospheric layer, where high temperatures prevail, is verified by the typically higher values of the rotational temperature obtained for H_3^+ than for H_2.

4.4. *Verification of Model Assumptions*

A key assumption in our model is that the line emission from H_2 occurs largely in a high-altitude layer. The high rotational temperatures (590–940 K) we derive for the emitting H_2 and the excellent simultaneous fit of the H_2 S and Q-branch line intensities support our assumption and indeed are strong evidence that the bulk of the line emission occurs well above the homopause, where hydrocarbons are absent. Moreover, the accuracy of the single temperature fit implies that the $v = 1$ level of H_2 is not significantly overpopulated, as it certainly is for Jupiter (500 times the LTE population), owing to auroral excitation (Kim et al. 1990). This as well as the global extents of both the H_2 and H_3^+

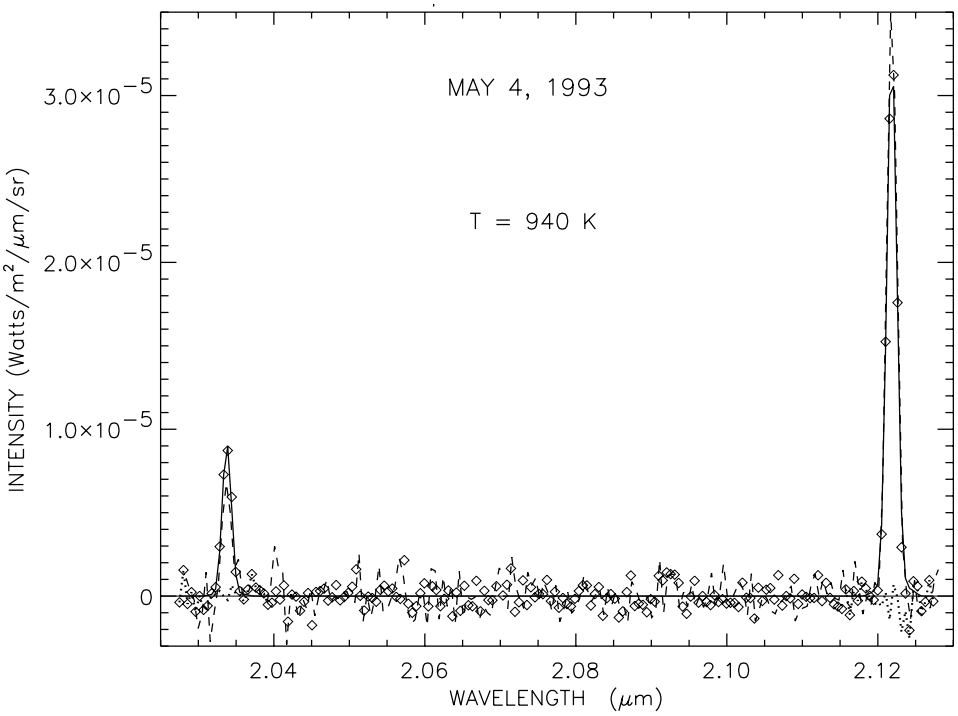

FIG. 10.—Fit of the synthetic H_2 spectrum of the $S(2)$ and $S(1)$ quadrupole lines to a spectrum of Uranus taken around 12:57 UT on 1993 May 4, when its hottest temperature, $T = 940$ K, was observed. This fit reveals a rotational temperature possibly hotter than the H corona. The residual is shown by the dotted line near the base of the emission lines. The dashed line is the 738 K spectrum taken on 1993 May 5 at relative phase 0.46, showing a different line ratio but a comparable excited H_2 column.

emission indicate that nonauroral processes dominate the excitation of each species.

5. THE ROTATIONAL PHASE VARIATION

The four consecutive nights of the 1995 UKIRT run provide longitudinal coverage of Uranus's emission spectrum during a quiescent period. Figure 11 plots the emission flux versus the relative rotational phase for the more prominent H_2 lines. The spectra were scaled to maintain a constant continuum flux through the slit; this corrects for nightly seeing differences since longitudinal cloud structure averaged along the central meridian is weak. The rotational phase variation of the emission intensities is seen to be slight. By coincidence, two of the rotational phases for H_2 nearly coincide. Their near agreement is a measure of the uncertainty in the fluxes.

Plots of the 1995 June rotational phase variation of the rotational temperature of H_2 and H_3^+ are compared with the corresponding H_3^+ vibrational temperature variation in Figure 12. The longitudinal variation of the H_2 temperature

TABLE 6

ROTATIONAL AND VIBRATIONAL TEMPERATURES FOR H_3^+

Date (UT)	T_{rot} [a] (K)	T_{vib} [b] (K)	$N(H_3^+)$ [c] (10^{15} m^{-2})	$E(H_3^+)$ [d] (mW m^{-2} sr^{-1})
1992 Apr 1	757 ± 25[e]	...	2.14	17.1
1993 May 3	751 ± 65	...	1.74	13.3
1993 May 4	735 ± 65	678 ± 10	1.74	12.2
1993 May 5	660 ± 65	...	2.74	10.4
1994 Jul 20	635 ± 65	...	3.79	12.1
1994 Jul 23	648 ± 75	...	4.28	14.1
1995 Jun 11	717 ± 70	552 (+60, −50)	1.56	9.37
1995 Jun 12	662 ± 70	490 (+50, −40)	1.94	7.74
1995 Jun 13	668 ± 70	511 (+50, −40)	1.91	7.66
1995 Jun 14	717 ± 70	519 (+50, −40)	1.43	8.60

[a] From the fundamental-band emission; the rms dispersion for 1995 is 691 ± 30, less than the measurement errors.

[b] From ratio of $v \rightarrow 0$ $R(6)$ line at 2.093 μm to the $v \rightarrow Q$ (1) line at 3.986 μm; The rms dispersion for 1995 is 518 ± 26 K; i.e., significantly less than the measurement errors.

[c] H_3^+ column density (ions m^{-2}) averaged over the disk assuming downward radiation is absorbed by the atmosphere; the vertical column could be as low as half these values depending on the degree of subsolar concentration.

[d] Frequency-integrated H_3^+ emission intensity weighted toward the center of the disk; The 1995 values correct erroneous values in Lam et al.'s 1997b Table 3.

[e] Trafton et al. 1993, refitted.

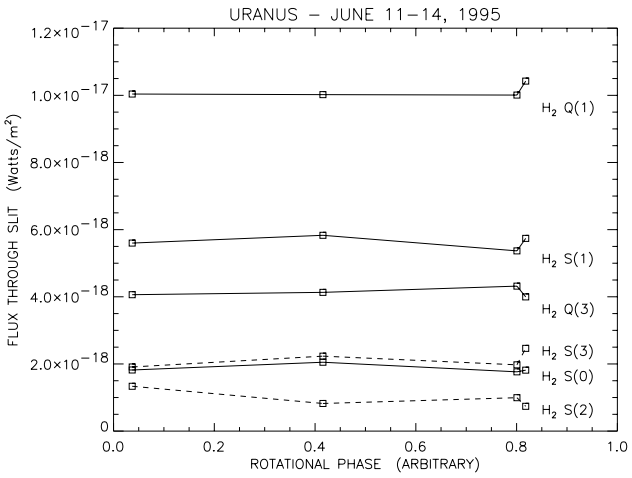

FIG. 11.—Rotational phase variation of Uranus's H_2 quadrupole emission fluxes during four nights in 1995 June. The dispersion in the nearly coincident phases provides an indication of the error. The dashed lines correspond to the two noisiest weak emission features.

is clearly statistically significant. Moreover, the H_2 and H_3^+ temperatures appear to vary in parallel even though the estimated rms error bars for the H_3^+ temperatures are larger than the temperature excursions, suggesting that the relative error is smaller than the indicated error. The longitudinal variations were subdued during this time, implying only weak auroral emission. Figure 12 also shows that the vibrational H_3^+ temperatures measured for 1995 are systematically lower than the rotational temperatures, measured for the same nights, by about 160 K. Therefore, Uranus's H_3^+ is not in vibrational thermal equilibrium, indicating that this ion is formed at atmospheric densities less than 10^{12} cm^{-3}, further confirming our modeling assumption that the H_3^+ emission arises primarily above the cooler regions of the thermosphere. This contrasts with Jupiter's case where H_3^+ appears to be nearly in thermal equilibrium (Miller, Joseph, & Tennyson 1990).

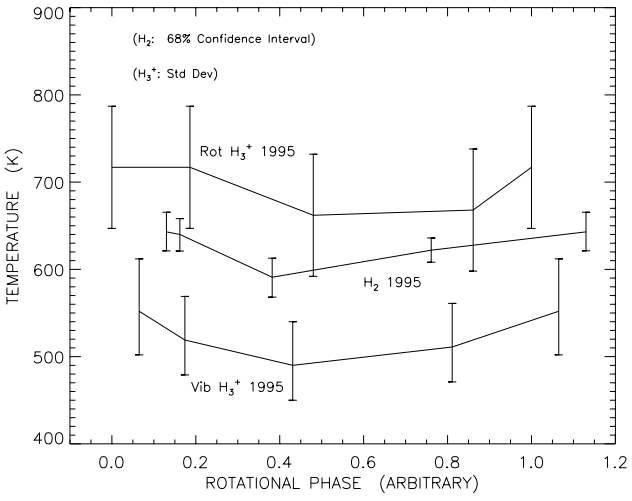

FIG. 12.—Comparison of Uranus's rotational phase variation of the rotational temperature of H_2 with that of H_3^+ and with the vibrational temperature of H_3^+ during 1995 June. The 90% confidence intervals are only marginally greater than the 68% ones (see Table 5). The temperatures appear to vary in parallel with rotational phase, possibly owing to a localized auroral component of the emission.

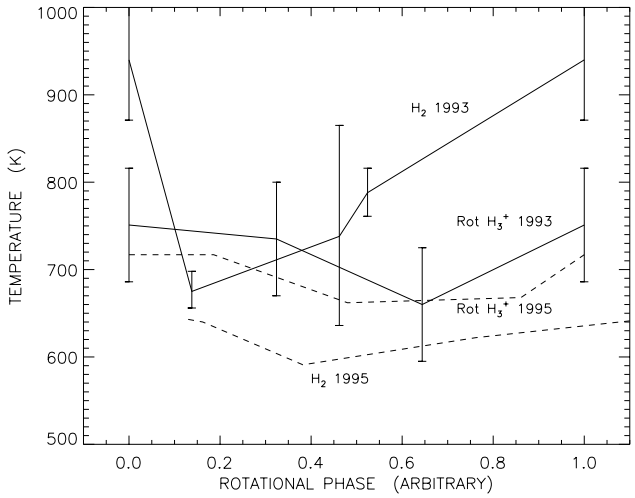

FIG. 13.—Early May of 1993 rotational phase variations of the H_2 and H_3^+ rotational temperatures. The phase difference with respect to Fig. 12 is unknown owing to the uncertainty in Uranus's rotational period, so the overplotted dashed lines for the 1995 data may contain an arbitrary phase shift. Nevertheless, the Uranian thermosphere was much hotter during the 1993 observations than during those of 1995. Time increases monotonically with phase in this figure, with the highest temperature occurring first. The value plotted at phase = 1 maps the zero-phase value to show the longitudinal variation (assuming the duration of the excitation was longer than a day).

Figure 13 plots the 1993 rotational phase variations for the H_2 and H_3^+ rotational temperature (*solid line*) and compares them with the 1995 values (*dashed line*). However, the phase relative to Figure 12 is arbitrary because of the uncertainty in the rotational period. Although the error bars of the H_3^+ rotational temperature are consistent with there being no rotational variation, the H_2 rotational temperature exhibits a large variation, with a value at one phase reaching or exceeding the H coronal temperature of 850 ± 100 K. In addition, the rotational temperature of H_2 (940 K) and the vibrational temperature of H_3^+ (678 K; Table 6) observed on 1993 May 4 are each higher than observed on any other night. The vibrational temperature for H_3^+ on this night lies closer to its rotational temperature (Table 6) than in 1995, suggesting that auroral excitation to the $v_2 = 2$ state occurred, populating it closer to the equilibrium value.

Comparisons such as this may eventually improve the accuracy of calculations of Uranus's rotational period and allow the relative phases of data from different apparitions to be calculated in order that they may be superposed on the same rotational phase plot. Being able to predict the rotational phase would also be useful for planning future observations of the aurorae. This comparison suggests that a longitudinal variation of the global emission may be a permanent feature, surviving changes in thermospheric temperature, but more data are needed to further characterize this variation and to separate the auroral and thermal emission components for further study.

6. THE LONG-TERM VARIATION

Uranus's H_2 emission was brighter, hotter, and showed greater extremes in 1992–1993 than in 1995. Values of the rotational temperature of H_2 ranging from 675 K to 940 K were derived from the 1993 May observations versus the 624 ± 24 K average found for 1995 June. Uranus's near-IR

H_2 line intensities were weaker in 1995 by nearly half of their 1993 values, and the rotational phase variation of the temperature was markedly less. Trafton et al. (1993) also reported detecting H_2 $S(1)$ line emission on 1992 May 5 with intensity 5.3×10^{-8} W m^{-2} sr^{-1}. This intensity is similar to the values reported here for 1993 (Fig. 5), and so this line is also stronger in 1992 than in 1995, like the H_3^+ emission. It appears that Uranus's thermosphere cooled between 1992 and 1995.

The H_3^+ emission appears to have been hottest in 1992, somewhat cooler in 1993 and 1994, and may have warmed slightly by 1995. Most H_3^+ emission intensities were significantly higher in 1993 and 1994 than in 1995, suggesting declining ionospheric activity over this period. The H_3^+ emission intensity in 1995 was about half that in 1992 (Trafton et al. 1993). The rotational temperature of H_3^+ was significantly lower in 1995 (691 ± 30 K [rms]) than in 1992 (757 ± 25 K) and was probably also lower during 1994 ($T \sim 641$ K). It appears that Uranus's ionosphere either cooled or suffered a decline in the excited column of H_3^+ between 1992 and 1995.

7. THE DISTRIBUTION OF H_2 AND H_3^+ EMISSION

The results of § 4.3 show that for 1995 June, most of Uranus's globally excited H_2 emission originated above atmospheric levels where the H_2 partial pressure was 0.10–0.21 μbar. This is consistent with the high values derived for the rotational temperature (averaging 624 K for the 1995 data) and the *Voyager* $T(P)$ structure below the top layer as well as the small H_2 column fitted to the line intensities. According to Figure 16 of Herbert et al. (1987), the altitude of the emission at the base of our top isothermal layer, corresponding to 500–530 K in the *Voyager* structural model, occurs 905–1100 km above an equatorial radius of 25,550 km. This implies emission beyond a planetocentric distance above the limb of 1.035–1.043 R_U where R_U is Uranus's projected radius. Since the atmospheric scale height for diffusively separated H_2 emitting at 624 K and 1.075 R_U is $\sim$335 km or 1.31% R_U, H_2 emission should be detected well beyond the limb, and a similar result is expected for the higher, ionospheric H_3^+.

We find that the distribution of H_2 emission along the slit, i.e., along the planet's CM, exceeds the planet's diameter by $\sim$10%. Our modeling indicates that the FWHM is insensitive to variations in the Gaussian seeing profile about a wide range of expected seeing values and is even less affected by the narrower instrumental point-spread function (PSF) and plausible tracking drifts. The observed FWHM is therefore a robust measure of the altitude extent of the emission. Our attempt to fit a model of the emission arising from a thin, homogeneously emitting shell located at the surface failed because the FWHM it predicts for the disk after convolving with the seeing and instrumental function is too small. Since this model predicts a CM emission profile that is too narrow for plausible seeing values, high-altitude H_2 emission is detected and resolved beyond the limb. Similarly, models with all the emission on the limbs can be ruled out because they cause the CM profile to have resolved lobes. Moreover, the 591–643 K rotational temperatures fitted for the 1995 observations correspond to emission above the 2000 km altitude level in the *Voyager* structural model, indicating that Uranus's upper thermosphere had warmed significantly since the *Voyager* epoch.

7.1. *Emission from an Elevated Shell plus a Hot Overlying Hydrostatic Layer*

The H_2 spectral emission model of § 4 is based on thermal emission from a series of isothermal concentric shells. This model implies a variation of the line-of-sight emission over the disk. For the purpose of further constraining the altitude distribution of the emission in the hotter layers, we modeled the emission as arising from a warm, isothermal, hydrostatic atmosphere overlying a cooler, emitting, isothermal shell that is elevated above the surface. Using the results of our above modeling of the 1995 UKIRT H_2 spectrum, we determined for each H_2 line the separate contributions of the vertical emission rate from the top isothermal layer and from the nonisothermal sum of the lower emitting layers. Most of the emission comes from the hot outer shell, as before, which still has a rotational temperature determined in § 4 (see Tables 4 and 5). The cooler inner shell is constructed to radiate the total emission from all the lower layers as determined from the multilayer modeling of § 4, but for simplicity the emission is assumed to originate uniformly throughout the shell. Then for each oblique line of sight along the slit, we combined these contributions after weighting them by the air mass enhancement according to the formulae in Appendix E, which describes the CM modeling.

In modeling the 1993 CM distribution of the emission observed with CSHELL, we have the disadvantage that the rotational temperature is unknown because this instrument can observe only one line at a time. So we do not know what fraction of the emission arose from the hot top layer or how deep this layer penetrated. We therefore assumed the same partitioning of emission between the hot and cooler levels as found for the average 1995 June observations with CGS4 and scaled the total emission to fit the observed profiles. In general, the CSHELL data required upward scaling of Uranus's modeled H_2 emission [27% for $Q(1)$ and 47%–82% for $S(1)$], confirming brighter H_2 emission in 1993 than 1995. We also scaled the 1993 CGS4 data this way. This approximation is not critical because of the minor contribution ($\sim$5%) of the lower levels in our model, especially for the brighter emission in 1993. No scaling adjustment was required to fit the 1995 CGS4 H_2 profiles because the modeled intensities were already based on fits to their corresponding spectra, which were averaged over much of the CM for the rotational temperature determinations.

7.2. *The Central Meridian Variation of* H_2

CM intensity profiles were modeled for the H_2 $S(1)$, $S(3)$, $Q(1)$, and $Q(3)$ lines and fitted to the 1993 IRTF and 1995 UKIRT K-band emission spectra. No CM plots are presented for the 1993 UKIRT spectra owing to the large CGS4 pixel size then, which covered 87% of Uranus's disk. We describe the H_2 results here; the H_3^+ results will be discussed in § 7.3.

The fits for the nightly averaged 1995 June CGS4 data are shown in Figure 14, which represents an average over four longitudes. The variation in the profile shape from line-to-line and night-to-night is partly due to the slightly different placement of the planet on the detector array relative to the detector rows. To obtain the nightly averages, the profiles were shifted to superimpose them at the FWHM points and then linearly interpolated at the June 11 diode locations. The interpolated profile has the same area as the

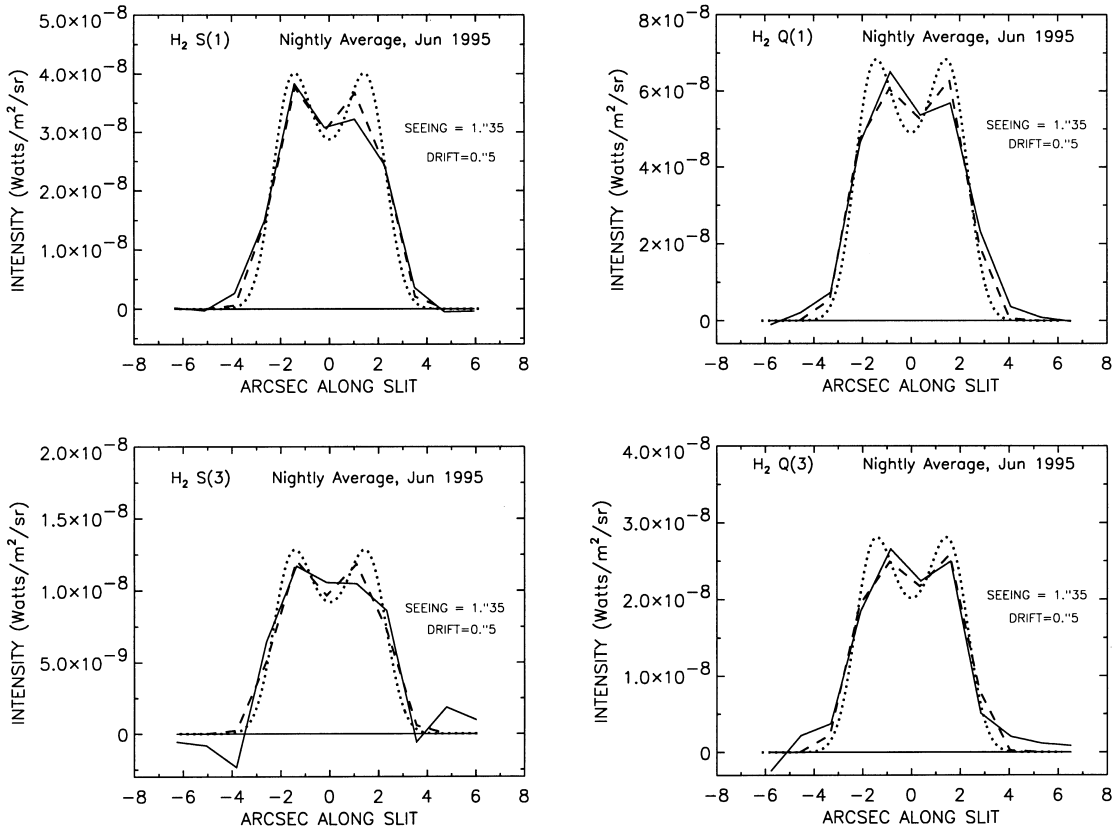

FIG. 14.—Comparison of Uranus's nightly averaged H_2 emission profiles for 1995 June vs. position along the central meridian with the fitted synthetic profile for a globally uniform thick-shell emission model. Uranian north and the equator are to the left. The dashed line is the modeled profile and the dotted line is this profile without the convolution with the CGS4 diode. In conjunction with the diode boundaries, it explains the irregular shape of the fitted profile. For these data, an average over several longitudes, the northern (low-latitude) limb appears to fit the model better; the southern (high-latitude) limb appears to have a systematic deficit of emission by comparison.

original profile. The resulting points were averaged to yield a mean profile, which appears to sample the diode array at a shifted position. All the modeled CGS4 profiles include a 0".5 drift representing the UKIRT tracking oscillation discussed above. Although the seeing varied nightly, we modeled these profiles assuming an effective average seeing profile. While the FWHM only weakly constrains the seeing, the seeing is quite sensitively constrained by the contrast of the two emission lobes. Fitting the nightly average profiles of these lines yielded an effective seeing of 1".35. This value is slightly higher than the ~0".8–1".2 estimated in the log.

A comparison of the observed nightly 1995 CGS4 profiles with the synthetic profiles that were fitted to the nightly averaged data is shown in Figures 15 and 16, respectively, for the $S(1)$ and $Q(1)$ H_2 lines. The limited S/N did not justify fitting the seeing for each night separately. It is clear from these figures that apart from a north-south asymmetry, the model reproduces the qualitative features of these profiles. It is also clear that the same FWHM fits the various rotational phases observed, so the altitude extent of the emission (at the limb latitudes sampled) does not appear to change with rotational phase. The FWHM of the CM profiles observed with each instrument are listed in Table 7. The FWHM of the nightly averaged CGS4 profiles for H_2 varies from 5".1 to 5".2 except for the weaker and relatively noisier $S(3)$ line, which has a less reliable apparent FWHM of 5".5. The brighter $Q(1)$ profiles have slightly better fits in the lobes, probably because of better S/N.

Figure 17 shows the fit of the modeled H_2 profiles to the two brightest observed CSHELL observations. The mismatch is more evident owing to the higher spatial resolution. The fitting benefits from the much smaller diode size than for CGS4 but suffers from the lower S/N. For these data, the observed lobe contrast suggests a model-dependent seeing of ~1".43, which is higher than the above logged estimates. However, guiding was less certain with CSHELL and hand corrections may have contributed significantly to the dispersion. In that case, a modeled drift larger than the minimal 0".15 assumed may be appropriate.

Comparison with the 1995 profiles in Figure 14 shows that the $S(1)$ intensity is anomalously strong relative to the $Q(1)$ line. The CSHELL $S(1)$ line observed on 1993 May 27 (Fig. 17*a*) is 82% brighter than the 1995 June nightly averaged $S(1)$ line and the CSHELL $Q(1)$ line (Fig. 17*b*) observed on May 26 (27° of rotational phase earlier) is only 27% brighter than for the 1995 observations of $Q(1)$. Moreover, the FWHM of the CSHELL $Q(1)$ line agrees with the model fitted to the 1995 data, but this FWHM is less than that of the CSHELL $S(1)$ line. The $S(1)$ observation on May 25 also is anomalously hot and appears to have this larger FWHM (Table 7). A hotter thermosphere at these longitudes is consistent with a greater scale height and, consequently, with a greater FWHM for this profile.

Both CSHELL profiles show a lack of symmetry of the northern and southern emission lobes (left and right lobes on the plots), which is opposite to that observed during 1995 (see Figs. 14–16). Since the sunlit southern pole is to

TABLE 7

APPARENT EXTENT OF EMISSION ALONG URANUS'S CENTRAL MERIDIAN

Night (UT)	Emission Band	Emission Extent [a] (arcsec)	Spectrograph
	H_2 Quadrupole Lines		
1993 May 25	$S(1)$	5.1	CSHELL 2 spectra
1993 May 27	$S(1)$	5.0	CSHELL
1993 May 26	$Q(1)$	4.7	CSHELL
1995 Jun average	$S(1)$	5.1	CGS4
1995 Jun average	$S(3)$	5.5	CGS4
1995 Jun average	$Q(1)$	5.2	CGS4
1995 Jun average	$Q(3)$	5.1	CGS4
	H_3^+ Manifolds		
1994 Aug 21	3.534 μm	3.8	CSHELL 2 spectra
1994 Aug average.....	3.534 μm	4.2	CSHELL 3 spectra
1995 Jun average	3.454 μm	4.5	CGS4
1995 Jun average	3.534 μm	4.2	CGS4
1995 Jun average	3.619 μm	4.6	CGS4
1995 Jun average	3.670 μm	4.3	CGS4

[a] The FWHM of the CM profile of the spectral line (CSHELL) or feature (CGS4) integrated over wavelength.

the right of center of the profiles (at positive arcseconds), the visible equator is to the left. The H_2 line emission on these nights does not have a symmetric profile along the CM as predicted by the model but shows a relative enhancement at the limb closest to the sunlit pole. Both the $Q(1)$ profile on May 26 and the $S(1)$ profile on May 27 show a deficit of emission over the limb closest to the equator relative to the globally uniform shell model. The rotational phase difference of these observations is 0.27, and it is not clear whether these differences exist at other rotational phases.

7.3. *The Central Meridian Variation of* H_3^+

CM profiles were measured for the 1995 CGS4 observations of the four spectral features of the fundamental

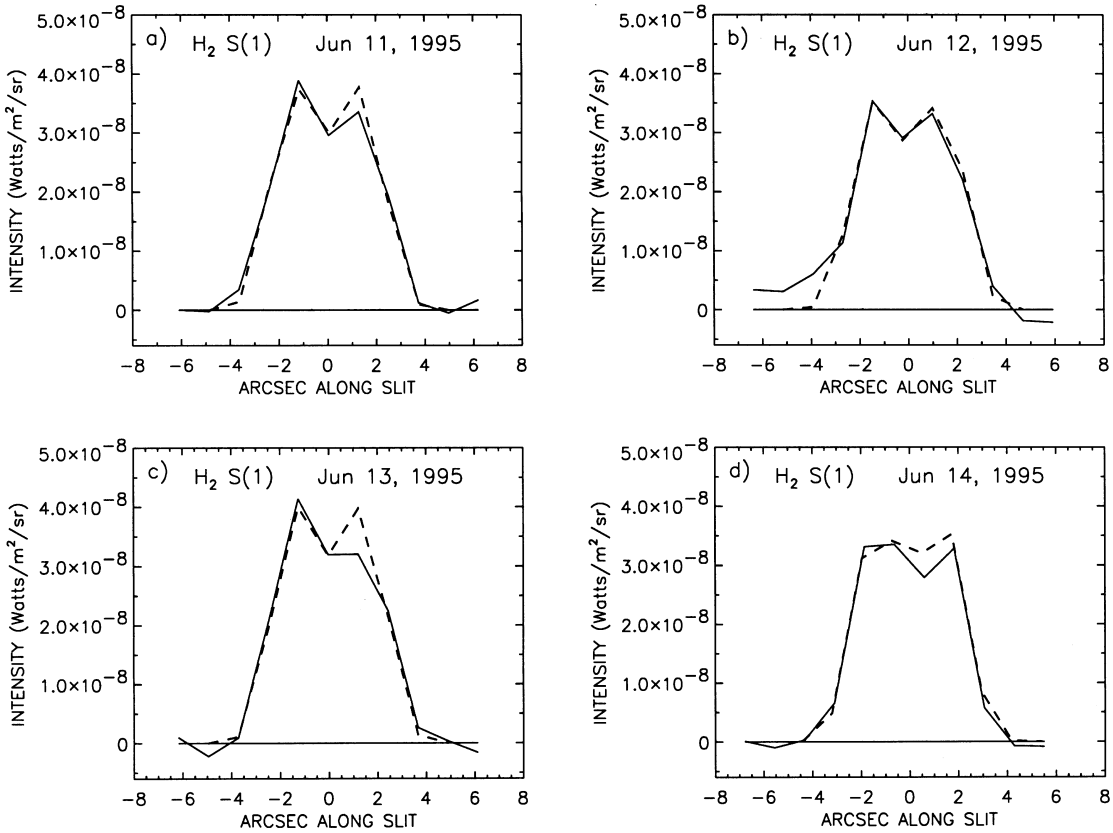

FIG. 15.—Comparison of the nightly $S(1)$ H_2 emission profiles for 1995 June vs. position along the central meridian with the synthetic profile assuming globally uniform emission and seeing 1".35. The synthetic profiles fitted to the nightly average data (Fig. 14) were rescaled to fit the nightly intensity variations. Note the good fits at FWHM and the qualitative agreement in the core.

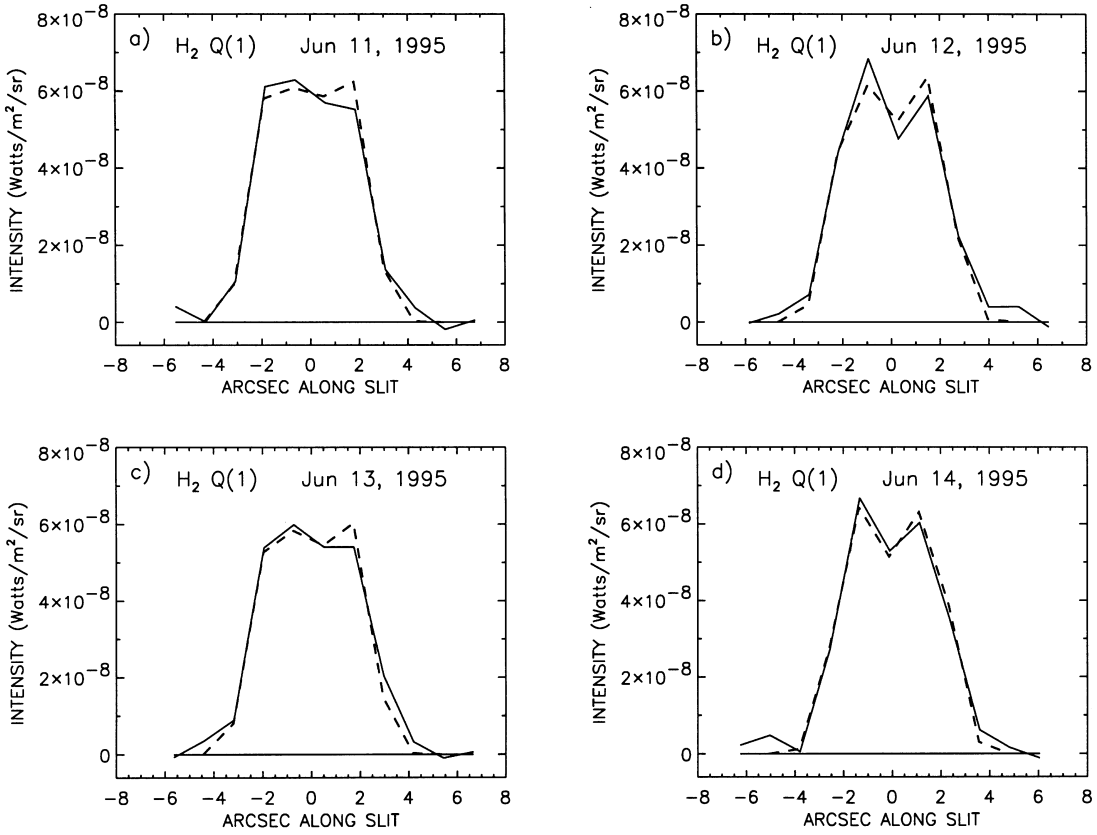

FIG. 16.—Same as Fig. 15, except for the $Q(1)$ H_2 line

band of H_3^+ listed in Table 8 and for the 1994 IRTF observations of the brightest line of the 3.534 μm H_3^+ band. The H_2 emission model fails to fit these profiles so it was modified in order to obtain a lower limit on the amount of central concentration of excited H_3^+, demonstrating the reality of this concentration. This model assumes that the emission originates entirely in a thin shell at the surface of the planet. It minimizes the bimodality of the profile due to the limb enhancement and so represents the limiting profile for emission from a globally uniform emitting shell.

7.3.1. *The 1994 IRTF Observations*

The profile for the average of the three 1994 August H_3^+ CM profiles plotted in Figure 6 is shown in Figure 18, for which the second and third observations were linearly interpolated at the diode positions along the slit of the first observation after shifting to align their half-maxima. Unlike for H_2, the average H_3^+ profile is clearly peaked near the center of the disk instead of at the limbs. Furthermore, its FWHM is 4.″2, compared to 4.″7–5.″1 for the CSHELL H_2

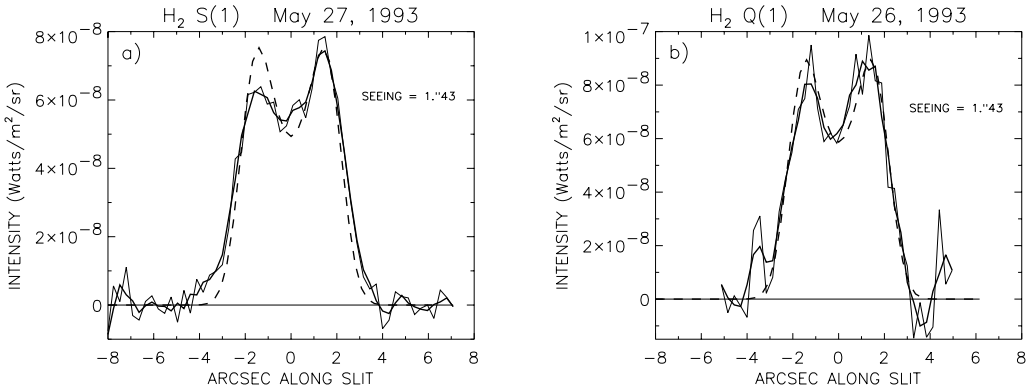

FIG. 17.—Comparison of Uranus's H_2 quadrupole emission profile during late May of 1993 vs. position along the central meridian observed with CSHELL with the scaled synthetic profile for a globally emitting thick shell: (*a*) the $S(1)$ line, (*b*) the $Q(1)$ line. The dashed line is the modeled profile and the observed profile is shown both unsmoothed and for a boxcar smoothing of three diodes. In contrast to Figs. 14–16, the northern (*left*) rather than the southern limb appears to be deficient in emission. The unusually bright (hot) $S(1)$ emission appears to have extended farther beyond the limb (i.e., to higher altitudes) than at the time of the $Q(1)$ observation.

TABLE 8

H_3^+ LINES INVESTIGATED

Wavelength (μm)	Transition	Laboratory Wavelength (μm)
3.454	5,3, − 1 → 4,3	3.455
	5,4, − 1 → 4,4	3.455
3.534	4,3, − 1, → 3,3	3.534
3.619	3,2, − 1, → 2,2	3.620
3.670	2,1, + 1 → 1,1	3.668
	2,0, + 1 → 1,0	3.669

profiles (see Table 7), confirming the greater concentration of this H_3^+ emission toward the center of the disk. Figure 6 indicates that the centralized concentration occurs for at least three longitudes in 1994, i.e., is probably a subsolar phenomenon. The longitudinal extent of the brightest component of this composite profile (Fig. 6, *dashed line*) is constrained by the fact that it occurred only 2:16 hr after the first observation, or 47° of planetary rotation later. A difficulty in explaining this brighter H_3^+ component in terms of auroral emission is that its peak appears near the center of the disk rather than being displaced toward lower latitudes (*left*) where the FUV aurora has been observed.

The dashed line in Figure 18 is the modified emission model calculated for a seeing of 1.″6, which is conservatively greater than the estimated 1.″1–1.″3. Its FWHM agrees with the averaged observations, suggesting that excited H_3^+ extends all the way to, but not significantly above, the limbs. The profile of the modified model still has bimodal peaks, in contrast to the observed single-peaked profile. The observed profile therefore indicates that excited H_3^+ in the $v_2 = 1$ vibrational state is concentrated toward the sub-Earth or subsolar point rather than being distributed more or less uniformly around the planet like the excited H_2.

7.3.2. *The 1995 UKIRT Observations*

The CM intensity profiles for the four selected H_3^+ spectral features listed in Table 8 and shown in Figure 3 were obtained by integrating each feature over wavelength for each row of the CGS4 detector array lying along the planetary spectral image. The nightly CM profiles for the four selected fundamental-band H_3^+ features are shown in Figure 19 for this run. These profiles were aligned relative to the third night along the slit by aligning their centroids computed above a threshold which excludes the extended wings. As observed for the H_2 emission, these profiles appear to indicate a subdued rotational phase variation, with a minimum also occurring on or near June 11 (*dashed line*). When areas are compared, the emission appears to be substantially stronger on June 14 (*dash–triple-dotted line*) than on the other nights, even for the noisier profiles. This is near the phase of the maximum H_2 temperatures observed, suggesting a common cause. The June 14 emission for 3.534 μm is not only the most intense at its peak, but also the broadest at its base. Therefore, its strength cannot be an artifact of better seeing on this date. During the first two nights, most features seem to be systematically enhanced on the northern limb, particularly the fainter ones.

In support of the results of the CSHELL H_3^+ observations, these profiles do not appear to be bimodal; most appear to be clearly peaked near the center of the disk, although the larger diode size tends to blunt the peaks. The profiles are shown with better S/N ratio in Figure 20 by averaging the nightly data (and longitudes) for each line. The profiles were first aligned as above then interpolated linearly at the diode locations along the slit for June 13. They clearly contrast with the usually bimodal H_2 profiles. In addition to their narrower FWHM widths (Table 7), another persistent feature is the asymmetry of these longitudinally averaged profiles; they appear to be biased toward the northern limb and/or the equator, perhaps reflecting a weak localized aurora, which would be manifest at low latitudes. We have attempted to model the most symmetric profile, the one for H_3^+ at 3.670 μm, in terms of a thin emitting shell at the surface, as we did for the CSHELL profiles, but instead using the CGS4 diode size and PSF, and the 0.″5 tracking oscillation derived from the K-band observations. A seeing of 1.″35 was conservatively assumed based on the K-band H_2 fits (the seeing should be better at L' than at K). The result is shown for the nightly data in Figure 21, where the model is the thick dashed line. The absence of emission extending significantly above the limb, given that the H_3^+ is hotter than the H_2, and the lack of a secant enhancement in the observations characteristic of thin-shell emission confirm that H_3^+ was concentrated toward sub-Earth or subsolar latitudes during 1995 June. Together, the CSHELL and CGS4 results imply this behavior during 1993–1995.

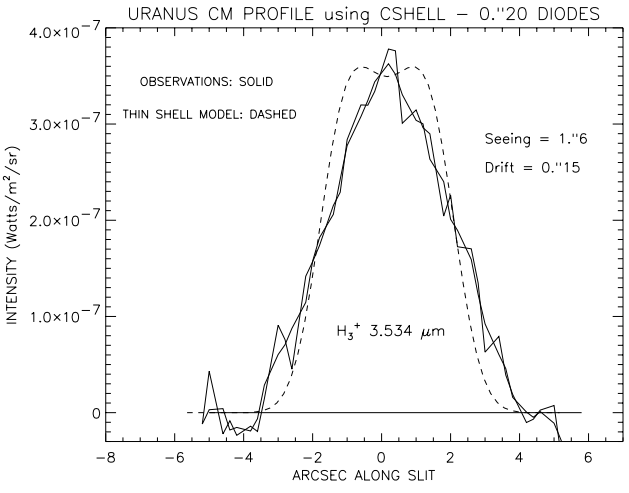

FIG. 18.—Comparison of the 1994 August average integrated intensity of Uranus's H_3^+ emission for the brightest line of the 3.534 μm manifold vs. position along the central meridian observed with CSHELL with the modeled profile for the limiting case of emission from a thin, uniform shell at the planet's surface (*dashed line*). The observed profile is shown unsmoothed and with boxcar smoothing of 3 pixels.

7.4. *Total Power Radiated*

Now that we have constrained the spatial distribution of the emission, the total power emitted by the planet (luminosity) in these species can be estimated. We estimated the luminosity of Uranus in the H_2 quadrupole lines by approximating the outward flux, referred to an effective emission altitude of 0.05 R_U above the planet's surface, by solid angle 2π sr times the fitted emission intensity at the center of the disk. This would yield the flux just above a thin emitting layer. We then multiplied this flux by the area of the corresponding sphere. This procedure assumes that absorption and scattering in the emission layer are negligible, that the downward flux is absorbed by the planet, and that the radiated flux is constant over the planet's surface,

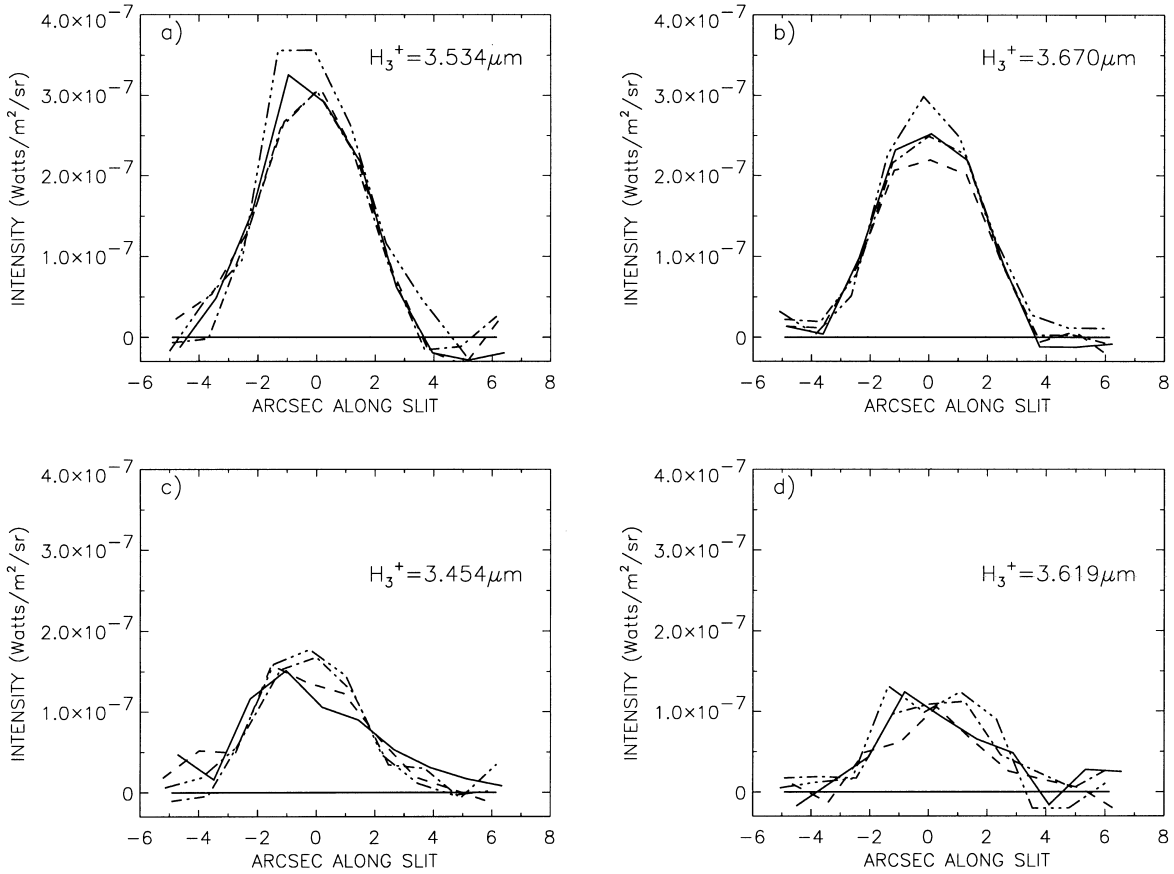

FIG. 19.—Comparison of nightly observations of the central meridian distribution of Uranus's H_3^+ manifolds taken by CGS4 in 1995. The June 11–15 observations are indicated by the solid, dashed, dot-dash, and triple-dot-dashed lines, respectively. The emission tends to be concentrated near the center of the disk, with a possible enhancement on the northern limb during the first two nights.

an assumption consistent with the results of fitting our thick-shell model. The total intensity was estimated by summing the integrated intensities of contributing lines of the *S*, *Q*, and *O* ro-vibrational branches, and the pure rotational *S* branch, of the fitted synthetic spectrum. In particular, *S*(0–5), *Q*(1–7), and *O*(2–9) were summed for the ro-vibrational lines and *S*(0–9) for the rotational branch. Since rotational temperatures are needed to estimate the emission from the nonobserved lines, only CGS4 data were used.

Over 90% of the IR H_2 quadrupole emission arises from the pure rotational lines, which is dominated by the cooler, lower levels where the temperature is more stable. About 70% of the emission comes from the $J = 0$ and $J = 1$ lines, which originate effectively just above the tropopause. For $J = 0$, the quadrupole H_2 line core reaches optical depth unity around the 4 mbar level at 67 K. The emission of the pure rotational lines from modeled layers above this level was therefore summed to estimate the power emitted by these lines. The rotational band emission in our model varied by only ~3% in response to the temperature changes between 1993 and 1995. The best luminosity estimate for the rotational band, 1.84×10^{11} W, was obtained for the nightly averaged 624 K spectrum observed in June 1995 (Fig. 9), because of the high S/N and Uranus's quiescence.

The power emitted by H_2 in the $v = 1$ level, which originates higher in the thermosphere, was 1.0×10^{10} W in 1995 compared to a value 60% higher in 1993. The luminosities for 1993 May 4 and 5 were about equal in spite of the higher (940 K) temperature on May 4. The higher temperature was offset by a thinner emitting layer. The luminosity in $H_2(v = 1)$ appears to be more stable than the thermospheric temperature.

The luminosity in H_3^+ during the 1995 run was estimated by correcting the average of Lam et al.'s (1997b) Table 3 values of $E(H_3^+)$ corresponding to the total H_3^+ emission flux referred to Uranus's surface for the ~20% light lost on the slit jaws for the calibration star observations and then multiplying by the area of the planet's disk. The nightside emission was neglected since the subsolar concentration implies that it is largely solar-induced. The area of the disk rather than the hemisphere was used as a crude approximation to the subsolar concentration. These and the Trafton et al. (1993) spectra were refitted to correct an error in the calculation of $E(H_3^+)$ and the column density. The corrected values are listed in Table 6 along with the values from the other years. The annual averages of $E(H_3^+)$ and the disk luminosity are listed in Table 9. The value of the H_3^+ luminosity during 1995 June is 1.1×10^{11} W (20% uncertainty with these assumptions). This implies that the total power emitted by Uranus's H_3^+ lines was 55% that radiated by the H_2 quadrupole spectrum in 1995 and 85% during 1993. The corresponding disk luminosity for Uranus from the 1992 April observations of H_3^+ by Trafton et al. (1993) is 2.2×10^{11} W, twice as high as for 1995. This factor-of-2 decline in Uranus's H_3^+ luminosity from 1992 to 1995 is significant and qualitatively agrees with the lesser decline in

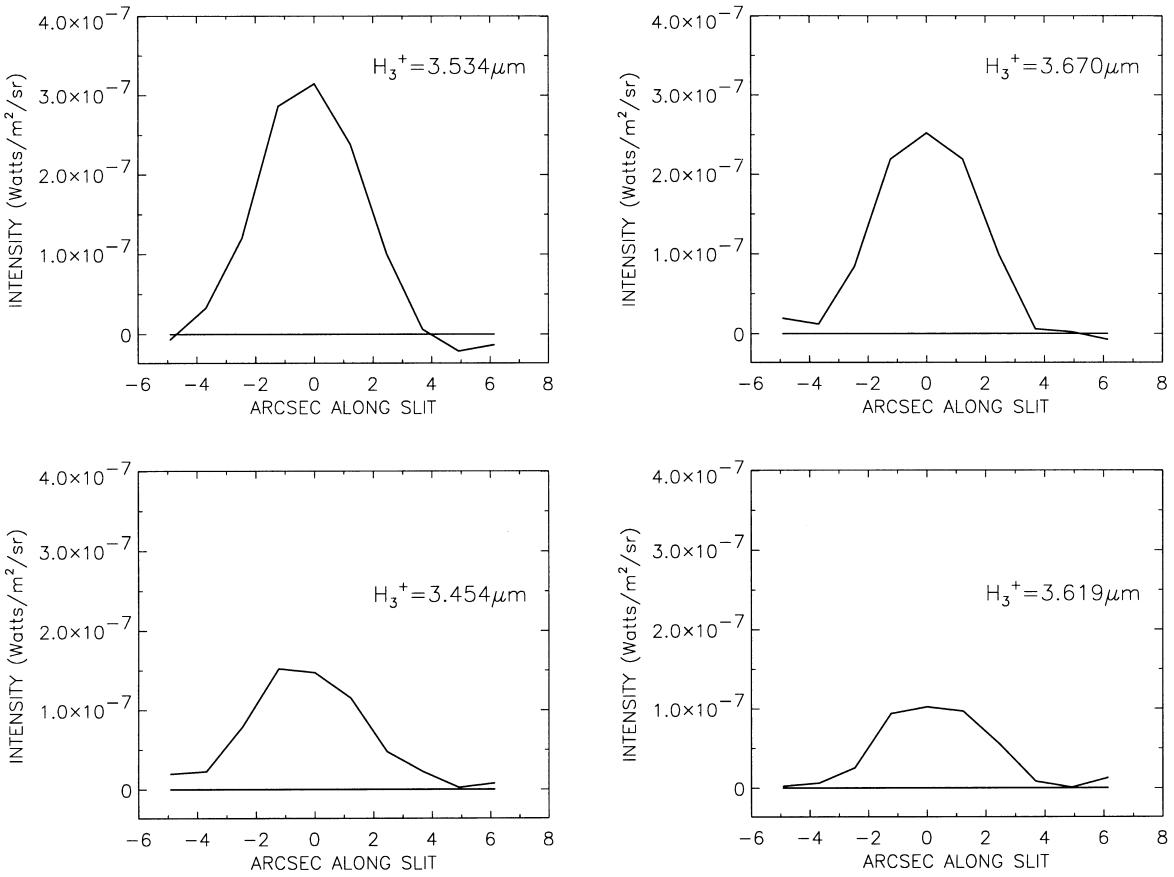

FIG. 20.—Comparison of the nightly average of observations of the central meridian distribution of Uranus's H_3^+ manifolds taken by CGS4 in 1995 June 1995. These higher S/N average emission profiles tend to be more symmetric than the nightly profiles, although 3.454 μm remains noticeably asymmetric.

the H_2 luminosity from 1993 to 1995. These values compare with $\sim 10^{13}$ W for the H_3^+ luminosity of Jupiter (Lam et al. 1997a).

The FUV/EUV input power of Uranus during the *Voyager* epoch near solar minimum may well have been $\sim 4 \times 10^{11}$ W (Broadfoot et al. 1986; Herbert & Sandel 1994; Trafton et al. 1993). Assuming a reasonable 10% conversion rate, this implies a total luminosity over all emission species of only $\sim 4 \times 10^{10}$ W. This is only 13% of the combined IR luminosities of H_2 and H_3^+ in 1995 June, also near solar minimum, and 10% of the combined luminosities observed in 1992–1993 near solar maximum. Therefore, the input power appears to have increased since the time of the *Voyager* flyby. The increase, however, probably is not as large as these percentages imply since the FUV input is unlikely to penetrate deep enough to explain most of the $S_0(0)$ and $S_0(1)$ emission. The IR emission appears to be brighter near solar maximum than minimum, but Uranus

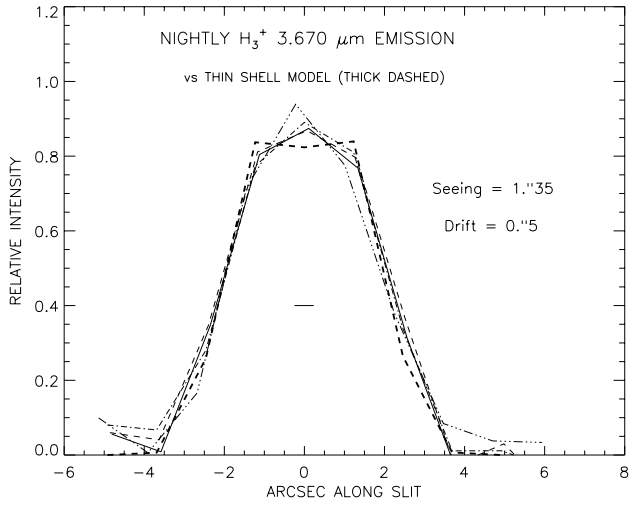

FIG. 21.—Comparison of normalized nightly observed and modeled central meridian distributions of Uranus's H_3^+ 3.670 μm feature taken by CGS4 (1."23 diodes) in 1995 June. The nightly profile code is the same as for Fig. 19. The model conservatively assumes emission from a thin, globally uniform, surface shell; i.e., no emission beyond the limb. The mismatch approaching the center of the disk implies that H_3^+ in the $v_2 = 1$ vibrational state is substantially concentrated near the subsolar region rather than being distributed more uniformly around the globe as for excited H_2.

TABLE 9

AVERAGE INTEGRATED H_3^+ INTENSITY AND LUMINOSITY FOR EACH YEAR

Year	$E(H_3^+)$ [a] (mW m^{-2} sr^{-1})	Global $E(H_3^+)$ [b] (W × 10^{11})
1992 Apr	17.1	2.20
1993 May.....	11.9 ± 1.4	1.54
1994 Jul.....	13.1 ± 1.4	1.70
1995 Jun.....	8.3 ± 0.8	1.07

[a] Annual averages of values in Table 6; errors are the standard deviation of the intra-annual values. The single 1992 point is uncertain by 10%. The rms average of the values in this column is 12.6 ± .

[b] H_3^+ luminosity of the sunlit hemisphere assuming that downward emission is absorbed by the atmosphere; values could be twice these if subsolar concentration were negligible.

appears to have been more active during the most recent solar minimum than the previous one during the *Voyager* flyby. Also supporting a solar cycle dependence of the H_3^+ luminosity is the greater emission versus rotational phase activity in 1992–1993 than in 1995.

7.5. *Discussion*

The observed thermospheric and ionospheric cooling and decline in emission intensity during 1992–1995 appears to have been driven by the declining solar activity during this phase of the solar cycle. The ionization potential of H_2 is 15.37 eV so that solar EUV with wavelengths less than 806 Å can produce H_2^+, which reacts with H_2 to form H_3^+. Changes in the solar EUV flux can then cause changes in the production rate of H_3^+ and hence in its excited column and emission intensity. Since the solar EUV flux varies throughout the solar cycle, one might expect there to be a solar cycle variation in the luminosity of H_3^+.

The parallel decline in H_2 and H_3^+ temperatures during this period would be consistent with the declining phase of the solar cycle if the emitting layers were primarily heated by solar ultraviolet radiation. The dissociation energy of H_2 is 4.48 eV, so that photons with wavelength less than 2767 Å can dissociate H_2 and so help to heat the upper thermosphere. The solar flux becomes increasingly variable over the solar cycle below about 2100 Å, varying about a factor of 2–3 in the FUV. The ionization potential of H is 13.60 eV, so photons below 912 Å can ionize H and so contribute to the periodic heating of the ionosphere over the solar cycle.

Uranus's H corona will tend to absorb sunlight below 912 Å, including photons below 806 Å required to ionize $H_2(v = 0)$ and produce H_3^+. We propose that partial absorption of solar EUV in Uranus's H corona is responsible for the observed concentration of H_3^+ toward the subsolar point. The path length through the corona, and the optical depth, is higher near the limbs of the planet than at the center, so that the production rate of H_3^+ falls off toward the limb in the absence of an auroral or other source.

For an empirical eddy diffusion coefficient of 50–100 cm^2 s^{-1} determined from Uranus's Lyα intensity during the *Voyager* flyby (Emerich et al. 1993), Uranus's modeled vertical H column density is 2×10^{17} cm^{-2} (Ben Jaffel et al. 1991). At the ionization limit (912 Å), the continuous atomic absorption coefficient for photoionization of H in the $n = 1$ state is 0.0626 $Å^2$ per atom (Kurucz 1970, p. 75). This implies a vertical optical depth of 1.25 in Uranus's H corona since essentially all the H atoms should be in the $n = 1$ state at 900 K. Because this cross section falls off approximately as the cube of the wavelength, the EUV absorption of the H corona at wavelengths of 806 Å ($\tau \sim 0.9$) and below, sufficient to ionize H_2 and produce excited H_3^+, is in the range to explain the central disk concentration of H_3^+ and the variation of H_3^+ production over the solar cycle. At solar zenith angle 60°, this optical depth will be 1.8. The ratio of the transmitted solar EUV at these locations will then be $\exp(-0.9) = 0.41$; so a $\sim$41% drop in H_3^+ production rate occurs from the center of the disk to near the limb, which is consistent with the observed peaked CM profile, assuming that the loss rate of H_3^+ is constant over the disk. Detailed modeling is needed for these observations to constrain the H corona further, but we conclude that solar EUV, filtered by Uranus's H corona, is the dominant source of excited H_3^+ on the planet. This implies that solar EUV is responsible for the long-term variation that we report for Uranus's H_3^+ emission. The photoelectrons resulting from the EUV photoionization of H_2 could be a secondary source of excitation and also contribute to the periodic heating.

The H corona itself and its opacity should also vary with the solar cycle. A well-known example is the solar cycle variation of Jupiter's H column inferred from the Lyα intensity variation (Atreya et al. 1982). This would tend to reduce, but not eliminate, the amplitude of the solar cycle variation of Uranus's H_3^+ production because the coronal changes would derive from solar EUV acting on the H_2 atmosphere at the base of the H corona.

7.5.1. *Discussion of* H_2 *Results*

The nearly global uniformity of the 1995 UKIRT data, both in the CM fits and in the limited rotational phase variation of the emission intensity and rotational temperature, suggests that this was a time of relative quiescence for Uranus's thermosphere. The base of the hot top layer in our model (at 500 K, 0.16 μbar; see Table 3) implies an effective pressure of $\sim$0.08 μbar for the top layer. The 591–643 K H_2 rotational temperatures derived from fitting the 1995 observations are significantly warmer than $\sim$535 K found by the *Voyager* UVS experiment at this effective pressure level and are actually more characteristic of the temperature at the nanobar level derived by *Voyager* (at over twice the altitude, i.e., 2700 km; see Herbert et al. 1987). Since our CM profile fits are not consistent with the higher emission altitude (0.10 R_U), this indicates that Uranus's thermosphere had warmed significantly since the *Voyager* epoch The increased scale height resulting from the higher temperatures found since the *Voyager* epoch would be expected to extend the atmosphere to higher altitudes, explaining the fit to the observed CM profiles.

But even for this quiescent period, rotational phase variations were detected in the temperatures of H_2 and H_3^+ and in the hot H_2 column (Figs. 12 and 13; Table 5). Aurorae are probably responsible for these and may contribute to the observed CM asymmetry neglected in the modeling. The subdued longitudinal variation of the emission flux (Fig. 11) suggests that the column of hot H_2 in the top layer (Table 5) is inversely correlated with the H_2 temperature. The insensitivity of the column density of emitting H_2 at different longitudes to the local temperature in 1995 (Fig. 11) was also the case during the run of early May of 1993, when higher temperatures redistributed the rotational level populations but did not cause a noticeable increase in the total emission. For example, Figure 10 suggests that the total excited H_2 column did not change appreciably with temperature between May 4 and May 5. A similar analysis of the Q branch for these dates indicated the same result. Auroral precipitation could account for this inverse correlation if its energy is deposited higher up in the thermosphere, where the temperature is higher and the total H_2 column is lower.

The unusually high 940 K H_2 temperature on 1993 May 4 may be a clear signature of the localized auroral H_2 emission reported by *Voyager* (Herbert & Sandel 1994). This temperature may even have exceeded the 850 ± 100 K coronal H value and contrasts with a much cooler temperature, 675 K, which was observed later that same night, with nonoverlapping error bars, at a different longitude

(Fig. 13). Because the auroral arc would be visible through the slit only near the northern limb for only a fraction of the period, the 2.5 times wider slit in 1993 resulted in a significantly higher probability of observing the aurora than during 1995. The higher H_2 than H_3^+ rotational temperatures observed at some rotational phases in 1993 is still consistent with the H_3^+ emission effectively originating at higher altitudes than the H_2 emission if the enhanced H_2 emission is largely aurorally excited. Aurorae deposit most of their energy near the deeper levels penetrated and so tend to heat those deeper levels more. Additional data showing whether such brightening is periodic with rotational phase would be useful for establishing whether localized auroral emission is indeed the excitation mechanism.

The greater spatial extent of the $S(1)$ line emission than of the less excited $Q(1)$ line observed at the IRTF in 1993 is consistent with elevated emission altitudes resulting from a higher temperature and the resulting greater H_2 scale height at the $S(1)$ longitudes. This effect was not observed in the 1995 data because of the milder temperature excursions then. During the interval between the 1993 and 1995 apparitions, both the excited H_2 column and temperature decreased significantly, as discussed above.

The 1995 H_2 emission appears to be variably brighter on the northern limb than predicted by the symmetric global model (Figs. 14–16). The opposite asymmetry in the strength of the H_2 lobes was seen for 1993 May where the southern lobe was brighter (Fig. 17). Since aurorae probably cannot brighten the southern lobe, these data may simply indicate a relatively cooler thermosphere in the northern (nightside) hemisphere, perhaps owing to the reduced diurnally averaged insolation at those latitudes.

Although our results for H_2 are consistent with thermal equilibrium, they do not exclude vibrational temperature deviations comparable to those observed for H_3^+. We were unable to determine the vibrational temperature of H_2 to establish whether a disparity exists in its thermal equilibrium. Specifically, we did not detect any of the S-branch lines of the (2–1) overtone of H_2, which lie in the K-band. The corresponding Q-branch lines lie just outside this band, beyond the spectral range observed. The (2–0) band emission should be even weaker against a brighter continuum. However, the much longer radiative lifetimes of the H_2 levels for these quadrupole emission lines than for H_3^+ favor thermal equilibrium to much lower densities than for H_3^+, as described in the next section.

7.5.2. *Discussion of* H_3^+ *Results*

On Jupiter, auroral H_3^+ is produced from H_2 ionized by particle precipitation (Drossart et al. 1989); its emission accounts for about two-thirds of the total planetary H_3^+ emission. Planetwide emission from H_3^+ is also observed, decreasing in intensity from about 25% of the auroral level at subauroral latitudes to a few percent of auroral at the equator (Ballester et al. 1994; Miller et al. 1997). This weaker emission is produced partly by solar EUV ionization of H_2. But there is an additional component that may be due either to transport from the auroral regions or from particle precipitation from the Jovian radiation belts (Miller et al. 1997). The populations of the fundamental, $v_2 = 1$, level and the overtone, $v_2 = 2$, level, are nearly thermal (Miller et al. 1990), and one may assume that a single, quasi-thermal, process serves to excite both. More recently, a latitudinal profile of the H_3^+ emission from Saturn shows that it, like Jupiter, is dominated by the auroral zones (Stallard et al. 1999).

By contrast, on Uranus the subsolar maximum of the fundamental H_3^+ emission suggests that this ion is being produced mainly by solar EUV ionization of H_2 (Waite et al. 1983), plus—as a secondary process—photoelectrons from the H corona, rather than auroral processes. This is in agreement with Lam et al. (1997b), who showed that auroral enhancement of the planet's emission is probably not greater than 20% of the total. At electron densities typical of the Uranian ionosphere, $\sim 10^4$ cm^{-3}, the chemical lifetime of H_3^+ is between 10^3 and 10^4 s, much less than the rotational period of the planet. This suggests that H_3^+ concentrations on the nightside should be low.

During the quiescent 1995 period, the rotational temperature of H_3^+ was systematically higher than that of H_2, indicating that H_3^+ was hotter. This indicates that the H_3^+ was effectively emitting at a higher altitude than H_2, or else the higher temperature arises from the subsolar concentration of this ion since the temperature is likely to be higher at this point. Although the lowest temperatures we have observed for H_3^+ occurred during 1994, when there were no H_2 observations, they are still higher than the lowest H_2 temperatures observed. The hotter H_2 temperature than H_3^+ observed in 1993 is probably a nonequilibrium phenomenon arising from auroral precipitation as on Jupiter, which overpopulates the $v = 1$ H_2 level more than the $v_2 = 2$ level of H_3^+ relative to $v_2 = 1$, in spite of the near-resonance between these species (see below).

The $(v_2 = 2)/(v_2 = 1)$ vibrational temperature of H_3^+ is normally significantly cooler than its rotational temperature and that of H_2. This suggests the ion is not in full ro-vibrational thermal equilibrium. This situation has been modeled for Jupiter by Kim et al. (1992). Schild et al. (1997) proposed that the collisional excitation rate for H_2 colliding with H_3^+ may be of the order of 10^{-10} cm^3 s^{-1}, based on a mechanism of "proton hopping" that converts the collisional energy into vibrational excitation of H_3^+; thus

$$H_2^* + H_3^+(v_2 = 0) \rightarrow H_2 + H_3^+(v_2 = v) .$$

The different thermal equilibria of these species can be easily understood by comparing the critical densities for the two molecules. H_2 radiative lifetimes are typically 10^7 s for the $v = 1$ level; those for H_3^+ are 10^{-2} s for both the fundamental and the overtone band (Dinelli et al. 1992a, 1992b). That means that the critical density at which collisional excitation is sufficient to populate the vibrational levels thermally is $\sim 10^6$ cm^{-3} for H_2, a density exceeded throughout the thermosphere, but is in excess of 10^{12} cm^{-3} for H_3^+, a density that is only reached close to the homopause, below the level at which peak H_3^+ production is most likely to occur. This is consistent with our proposal that $H_3^+(v_2 = 1)$ is being produced primarily by photoionization of H_2 or by photoelectrons, peaking above the subsolar point. For Jupiter, this process is most efficient at the nanobar pressure level, where densities are 10^{10} cm^{-3} or less (Waite et al. 1983).

However, Kim et al. (1992) also point out that the near-resonance of $H_2(v = 1)$ and $H_3^+(v_2 = 2)$ may contribute to populating the $v_2 = 2$ level. Thus, the resonant excitation of H_3^+,

$$H_2(v = 1) + H_3^+(v_2 = 0) \rightarrow H_2(v = 0) + H_3^+(v_2 = 2) ,$$

may become increasingly important in the case of Uranus, where "normal" collisional excitation of the H_3^+ vibrational levels is clearly inefficient owing to low number densities. One might reasonably expect, therefore, the CM distribution of $H_3^+(v_2 = 2)$ to reflect *both* the H_3^+ production profile, given by the CM distribution of $H_3^+(v_2 = 1)$ (Figs. 18–21) and that of $H_2(v = 1)$ (Figs. 14–17). Unfortunately, the CGS4 H_3^+ overtone data were too noisy to determine details of the CM profile for the $v_2 = 2$ level.

8. CONCLUSION

This study of Uranus's near-IR emission has demonstrated the importance of comparing the outer planets with one another. H_2 and H_3^+ emission from Jupiter has been well characterized, and both molecules show strong spatial variation. For Jupiter, the spatial differences are primarily between those regions that are dominated by auroral emission, around the magnetic poles, and the rest of the planet: H_3^+ emission from the body of Jupiter is at most a few percent of the auroral intensities, and H_2 nonauroral IR quadrupole emission is not yet detected, although its auroral emission is relatively strong.

In contrast to Jupiter, the emission from Uranus appears more evenly distributed across the planet. To summarize, Uranus's H_2 emission appears to be thermally induced by an extended hot thermosphere of the sort detected by *Voyager*. There is no indication that Uranus's thermospheric H_2 departs from thermal equilibrium; the extent of the emission beyond the limb is consistent with the large H_2 scale height associated with the high thermospheric temperature and thermal emission. The high thermospheric temperature probably results from the low homopause and corresponding lack of radiative cooling by hydrocarbons. This would be consistent with the lack of detection of planetwide H_2 emission from the other major planets, including Neptune. The thermospheric H_2 emission on the night side is likely to be as strong as on the dayside. By contrast, the slightly warmer $H_3^+(v_2 = 1)$ emission, although it covers the sunlit disk, appears to be concentrated toward the subsolar point and the population of H_3^+ in this state appears to be vibrationally relaxed relative to thermal equilibrium. While Uranian H_2 vibrational populations are thermalized, those of H_3^+ are not; the $v_2 = 2$ level is significantly underpopulated compared to $v_2 = 1$, giving vibrational "temperatures" usually much lower than the rotational temperatures derived for $H_2(v = 1)$ and $H_3^+(v_2 = 1)$. No H_3^+ emission was detected beyond the limb. Excited H_3^+ thus appears to be formed primarily by solar EUV light over a time interval small compared to the planet's rotation period. In this case, the nightside emission of H_3^+ is predicted to be much dimmer; i.e., relegated to auroral emission. We ascribe the relative lack of spatial variability on Uranus to the weakness of any auroral component relative to the planetwide emission, confirming the conclusions reached by Lam et al. (1997b) for H_3^+.

We conclude that Uranus's H_3^+ will not be in thermal equilibrium for densities less than 10^{12} cm^{-3}, but H_2 is likely to be in thermal equilibrium for densities down to 10^6 cm^{-3}. The resonant excitation of $H_3^+(v_2 = 2)$ by $H_2(v = 1)$ is therefore significant. As a result, the CM distribution of $H_3^+(v_2 = 2)$ should be sensitive to that of $H_2(v = 1)$, leading to more limb enhancement than is observed for $H_3^+(v_2 = 1)$, which peaks at the subsolar point. Unfortunately, the S/N of the overtone H_3^+ lines is not high enough to obtain a rotational temperature of the $v_2 = 2$ state. This would be of interest for comparison with the $H_2(v = 1)$ rotational temperature to investigate the influence of H_2 resonance. Further observations of Uranus are needed to investigate the resonant interaction of these species.

Apart from an unusually high temperature on 1993 May 4, we find limited evidence of auroral activity in Uranus's H_2 emission in the form of longitudinal temperature excursions. So it is likely that auroral emission does occur at levels that are detectable by ground-based studies and that increased effort is required to monitor this still poorly understood planet. New developments in IR spectrometers and cameras should assist such activity considerably. It will, surely, also be profitable to attempt correlated multiwavelength programs, particularly those that allow H_2 and UV H Lyα emission to be monitored simultaneously with the IR lines presented here.

We thank the staffs of the NASA Infrared Telescope Facility and the United Kingdom Infrared Telescope for their support of this work. UKIRT is operated by the Joint Astronomy Centre on behalf of the UK Particle Physics and Astronomy Research Council. We also thank Rene James for help in the reduction of the CSHELL data and D. F. Lester for extracting spectra from the HITRAN database. Support for this work was provided by NASA through grants NAGW-2314, NAG5-4934, and NAG5-6754, and by PPARC through grant GRK97837.

APPENDIX A

DETAILS OF THE OBSERVATIONS

During our observations, Uranus's spin axis was aligned nearly in the Earth's east-west direction. The planet's rings did not occult the emission. The south pole (IAU convention) is the visible pole, which is on the east side of the image. Viewed from above this pole, the planet rotates counterclockwise. For the CSHELL spectra, the position angle of the 1″–2″ wide slit was 95° for 1993 and 90° for 1994. For the 1995 CGS4 spectra, the 1.″35 wide slit was oriented at 90°.

Following Herbert et al. (1987), we adopted an equatorial radius for Uranus of 25,550 km. For a fluid planet, Uranus's rotation causes an oblateness of 2.29%, for which the polar radius is 24,965 km. The projected radius of the planet is intermediate between these values. Uranus's apparent equatorial diameter was 3.″64 and 3.″70 during our 1993 and 1995 observations, respectively. Correcting for the sub-Earth latitudes of $-56.^\circ5$ and $-48.^\circ8$, we derived values for the apparent CM diameter of 3.″61 and 3.″66, respectively. The spin axis is tilted nearly into its orbital plane, and the offset magnetic pole is tilted $\sim 60^\circ$ relative to its spin axis. With this geometry, Uranus's rotation modulates the observable auroral emission arising from the fragmented arc around the sunlit magnetic pole.

In 1993, CSHELL used a Rockwell NICMOS-3 detector array (0.″28 per diode) and in 1994, a 256 × 256 InSb array (0.″20 per diode) made by Santa Barbara Research Corporation. According to the slit width used, the spectral resolution for the CSHELL observations varied from 10,800 to 21,500 (Table 1). Owing to the small spectral bandpass, only individual H_2 or H_3^+ lines were observable; separate observations were required for each line. Because of this, and since only one H_3^+ line was observed, reliable rotational temperatures could not be extracted from the CSHELL data. On the other hand, CSHELL gave superior spatial resolution along the CM for detecting localized auroral emission owing to its smaller pixel size. However, this advantage was weakened by the worse than average seeing (~1″–1.″3) and the fewer Uranian photons collected by the smaller pixels.

The 1993 CGS4 observations employed a 58 × 62 InSb array made by SBRC with a diode size of 3.″08 square and a slit width to match. The 1994 observations, of the L' band only, employed the same detector with each diode projecting to 1.″54 on a side, matching the slit width. The extracted spectra for this year are the sum of three rows of the array covering a 1.″54 × 4.″62 area of sky. The 1995 observations employed a newly installed 256 × 256 InSb array made by SBRC yielding a pixel size of 1.″23 square with a slit width about 10% wider. The resolving power ranged from 340 in the case of the 1993 K-band survey to 1500 for the 1995 L'-band spectra (see Table 2). The 1995 K-band observations had a bandpass of 0.67 μm, which covered the whole K band. Hence, all the prominent H_2 lines and several weak features from the first-overtone band of H_3^+ could be recorded simultaneously, permitting the determination of rotational temperatures as a function of rotational phase of the planet.

Most observations were made in the "stare and nod" mode and lasted on the order of 1 hr. The telescope was nodded 15″–18″ for CSHELL and 12″ (10 integral detector rows) for CGS4 along the slit direction so that object and sky observations were always obtained simultaneously. The observing sequence produced successive quads of object-sky–sky-object spectra on one side of the slit, and sky-object–object-sky spectra simultaneously on the other side. To avoid aliasing and effects of bad diodes, each CGS4 spectrum was stepped in wavelength to sample two adjacent diodes over six equal steps. The basic 1995 Uranus K-band exposures were 10 s per integration, and the exposures were 0.15–0.2 s for the L'-band observations. For CSHELL, autoguiding was problematic, so guiding was done by hand using a TV guider, with corrections made while the planet was in the "Sky" nod-position. For CGS4, tracking on the planet and stars was maintained by an autoguider with the gain adjusted to make Uranus look like a point source. However, CGS4 suffered from a 1 Hz oscillation in right ascension with amplitude ~0.″5, which was only partially removed by the autoguider. Since the slit of the telescope was aligned in the east-west direction in 1995, this contributed slightly to the smearing of the observed CM intensity distribution which, however, was dominated by the 1.″23 diode and seeing. For 1993, the effect of this oscillation was much less owing to the 3.″1 diodes and the north-south slit orientation employed.

APPENDIX B

ABSOLUTE CALIBRATION

B1. IRTF SPECTRA

The telluric transmission for CSHELL's narrow bandpass was derived from observations of nearly solar-type standard stars using a 4″ wide slit. Since the seeing was typically better than 1.″3, little light should have been lost on the slit jaws (<0.1%), assuming that the star was approximately centered in the slit. The standard stars used were BS 7061 (F6 V, $K = 3.06$, $L = 3.03$, $T_e = 6270$ K), and BS 8430 (F5V $K = 2.69$, $L = 2.59$, $T_e = 6530$ K) (Koorneef 1983). A blackbody spectrum normalized to the star's K or L magnitude and having an effective temperature estimated from the standard star's spectral class (Allen 1976; UKIRT website table) was compared with the observed spectrum of the star to calibrate the observed count rate per diode in terms of absolute flux units. The location of the star on the detector and the nod angle were the same for both the star and Uranus. After evaluating Uranus's spectrum in flux units, we converted to intensity units by dividing by the solid angle defined by the diode height along the slit times the slit width. Since the inoperative rows of the array during the 1994 observations scaled the star and planet fluxes nearly equally, the observed count rate was not corrected for their inoperation. Such rows were skipped over in the plotting and analysis.

B2. UKIRT SPECTRA

For the 1993 UKIRT observations of Uranus, the absolute emission intensity was estimated from spectra of the flux-standard star BS 7340 (F0 IV–V, $K = 3.37$, $L = 3.36$, $T_e = 7020$ K). With a 3.″08 wide slit, the throughput was better than 99% for a Gaussian profile having FWHM equal to the estimated seeing. We converted Uranus's spectra from count rate to intensity units as described above for CSHELL, but for a diode size of 3.″1 square, matching the slit width. Differences in extinction arising from differences in air mass were neglected since their effect was less than other uncertainties in the flux calibration, which we estimate at 15%–20%. In 1994, L'-band spectra were obtained using CGS4 with 1.″54 square pixels and a slit width of 1.″54. The flux standards were BS 7264 and BS 6998. The flux was summed over three rows of the array covering a 1.″4 × 4.″ area of sky.

The absolute calibration of the nightly spectra for the 1995 L'-band observations of H_3^+ is based on Lam et al. (1997b), with a correction to account for their neglect of the partial transmission of the standard star flux through the 1.″35 wide slit. If the L'-band seeing was 1.″25, a value consistent with the average K-band seeing of 1.″35 fitted below for these same nights, the stellar slit transmission was 80%. We have therefore corrected their fluxes downward by 20%, and the intensity scale of Figure 3 includes our correction. The L'-band seeing and slit transmission could not be determined more accurately because of the

lack of a satisfactory model of the central meridian distribution of H_3^+ (see § 7.4). We checked the Lam et al. flux calibration for the 1995 L'-band observations using the B1 V star BS 5993 ($L = 4.13$, $T_e = 25{,}600$ K) observed on the same nights. Overall, the absolute calibration is about 20% uncertain owing to the intrinsic uncertainties in the calibration process.

The uncertainty in the absolute calibration does not affect our derived rotational temperatures for H_3^+ since these depend only on the ratios between the lines; nor does it affect the distribution of H_3^+ along the CM. But it does affect the determination of the H_3^+ column density and thus values of the total H_3^+ emission, $E(H_3^+)$, quoted in previous work (Lam et al. 1997b). Our flux calibrations for the 1993 and 1994 spectra were more accurate than that for 1995, owing to the larger apertures used.

APPENDIX C

SUBTRACTING THE CONTINUUM SPECTRUM

Since we are concerned here with investigating only Uranus's narrow emission features, we subtracted Uranus's underlying spectrum (hereafter referred to as its continuum) from each observed spectrum (whether or not a continuum was apparent). The continuum is affected by the broad pressure-induced H_2 absorption, pressure-broadened CH_4 bands, and scattering from gas and aerosol haze. The process involved subtracting a polynomial fitted to the continuum or background independently for each detector row across the nod-averaged image (the continuum spectrum varies with latitude). For the broadband CGS4 observations, a high-order (35–50) spline polynomial was used to fit and subtract the continuum. For the narrowband CSHELL spectra, a low-order (5) spline polynomial was used.

In subtracting the continuum, we neglected the narrow H_2 quadrupole absorption lines, such as those seen for the (3–0) and (4–0) overtone bands (e.g., Trafton 1976, 1987). These lines are highly saturated with equivalent width on the order of the Doppler emission width. However, the equivalent widths of the emission lines are so much greater than those of the absorption lines that the resulting error is less than $\sim 4\%$ of the observed emission strengths for the weaker H_2 lines and less than $\sim 1\%$ for the stronger lines. This estimate is based on the fundamental-band absorption-line strengths (Birnbaum & Poll 1969) and the H_2 column over the stratospheric haze responsible for the observed albedo in the strong pressure-induced bands. Similarly, we neglected any structure in the CH_4 spectrum in removing the background continuum. Such intrinsic structure is likely to be subdued because CH_4 is largely frozen out of Uranus's upper atmosphere, so that the observed bands are significantly pressure-broadened. The branch most affected by CH_4 would be the H_2 Q branch, near 2.4 μm, for which the background CH_4 absorption is strongest. The $S(1)$ line is free from any significant CH_4 contamination.

The Doppler shift of Uranus was such that none of the Q-branch emission features were selectively attenuated by telluric water or telluric methane lines according to the HITRAN molecular spectroscopic database (Rothman et al. 1996). Since these and the S-branch lines are narrower than the resolution element, we checked their Doppler-shifted wavelengths to insure that they did not fall near the cores of any telluric line detectable in a high-resolution solar atlas (Mohler et al. 1950). Although clear of the line cores of a strong telluric CO_2 band, the $S(3)$ line is partially absorbed by the wings of neighboring saturated CO_2 lines.

APPENDIX D

CALIBRATION OF THE 1995 CGS4 OBSERVATIONS

During the 1995 June observing run at the UKIRT, observations of standard stars were made using a 1.″35 wide slit on the CGS4 spectrograph. Consequently, the flux calibration determined from them is uncertain because of the seeing-dependent throughput. Nightly changes in the seeing also affect the nightly relative calibration and the comparison of the emission versus rotational phase. This Appendix describes the procedure used to correct for these effects.

Comparison of stellar profile widths along the slit measured from spectral images taken nightly during this run with their extracted count rate spectra indicates that essentially all of the nightly differences in stellar count rate were due to changes in seeing rather than to extinction changes, even on the night of June 12, when thin cirrus was noted. Note that the 1 Hz oscillation in right ascension of the telescope drive did not affect the slit throughput because the oscillation occurred along the slit. This conclusion is supported by integrations of Uranus's continuum along the slit, which is expected to be rotationally invariant in the K band apart from very small clouds occasionally transiting the central meridian which are primarily visible when they are on the limb (Karkoschka 1998). The count rates from the planet and the star are equally sensitive to extinction, but the count rate from the planet is significantly less sensitive to seeing and guiding errors because Uranus is a quasi-extended source relative to the slit width. Therefore, we did not explicitly account for the extinction differences arising from different air mass and transparency in the flux calibration.

However, we accounted for spectral differences in the nightly extinction of the 1995 observations by dividing the broad K-band Uranus spectrum obtained on each night by a spectrum of BS 7205 obtained on the same night. This F5 IV–V star was conveniently close to Uranus, so that the division cancelled out the telluric absorption over the K band and partially cancelled some solar features, which are weak compared to the telluric ones. The resulting individual Uranus spectra were then scaled to agree in continuum flux integrated over the slit with the Uranus spectrum of June 14, the night of best seeing. This removed the effect of nightly changes in the seeing and any residual extinction differences.

BS 7205 was used as a secondary standard ($K = 5.14$, $T_e = 6530$ K) calibrated at 2.18 μm by the primary flux standard star BS 8402 (B7 IV, $K = 4.80$ mag, $T_e = 13{,}100$ K; Gezari et al. 1993) observed only on the first night. The seeing is uncertain in

spite of measuring the star profiles along the slit because of the uncertainty in the instrumental imaging point spread function and in the amplitude of the 1 Hz oscillation. The uncertainties in the nightly variation of the seeing contribute to the uncertainty in the slit throughput leading to an unacceptably large (30%) uncertainty in the absolute flux. Therefore, we adjusted the scale of Uranus's 1995 spectra so that their common *continuum* intensity agreed with that of our well-calibrated 1993 May Uranus spectrum. We did this by averaging the nightly averaged 1995 continuum intensity in the three rows of the array centered on Uranus's image (sampling 1.″35 × 3.″7, the same height as Uranus's unsmeared diameter) and scaling the result to fit the 1993 disk continuum intensity averaged over the 3.″08 square diode centered on the planet. Provided that there was no change in Uranus's continuum albedo over that 2 yr period, this rescaling introduces error only from the (3×) difference in the image areas being compared, which we expect to be minor compared to the other uncertainties in the absolute calibration. We estimate the total uncertainty of the 1995 *K*-band intensities derived for Uranus's seeing-smeared disk to be 20%.

APPENDIX E

EMISSION FROM A HOT ISOTHERMAL HYDROSTATIC GAS LAYER OVER A COOLER ISOTHERMAL ELEVATED SHELL

The contribution to the observed emission by each of the two thick, contiguous shells depends on whether the line-of-sight "impact parameter" r is entirely in the hot outer shell (case 1), below the limb (case 2), above the limb but below the elevated inner radius of the finite cool shell in the plane of the sky (case 3), or above the inner radius of the finite shell but below its outer radius (case 4). The adopted inner radius of the cool shell is $R_{\rm in} = 1.015\ R_{\rm U}$ based on the rapidly falling temperature with decreasing altitude below this radius. The adopted outer radius of this shell and base of the hot isothermal shell is $R_{\rm out} = 1.039\ R_{\rm U}$ based on fits to the average 1995 observations.

For the top shell (case 1), we adopted a barometric density distribution valid when the scale height is small compared to the planetary radius. The tangential emission rate for paths lying entirely in the top shell, $r > R_{\rm out} = 1.039\ R_{\rm U}$, is

$$I(r) = \sqrt{\frac{2\pi r}{H}} \exp\left(-\frac{r - R_{\rm out}}{H}\right) E_1 ,$$

where E_1 is the vertical emission rate of the top shell for the line of interest and $H = 0.538\ T_{\rm rot}$ is the H_2 scale height in km at $1.075\ R_{\rm U}$.

For case 2, $r < R_{\rm U}$ in the plane of the sky, the contribution of the inner shell is

$$\frac{\sqrt{R_{\rm out}^2 - r^2} - \sqrt{R_{\rm in}^2 - r^2}}{R_{\rm out} - R_{\rm in}} E_s ,$$

where E_s is the vertical emission rate for the line of interest from all the cooler layers below the top one. The contribution of the outer shell is

$$\frac{R_{\rm out}}{\sqrt{(R_{\rm out}^2 - r^2)}} E_1 .$$

For case 3, $R_{\rm U} < r < R_{\rm in}$, the contribution is twice that of case 2 since both the front and back shells contribute to the observed emission.

For case 4, $R_{\rm in} < r < R_{\rm out}$, the contribution of the inner shell is

$$2\,\frac{\sqrt{R_{\rm out}^2 - r^2 + 0.02}}{R_{\rm out} - R_{\rm in}} E_s$$

and the contribution of the outer shell is the smaller of the following two expressions evaluated at r:

$$\frac{2R_{\rm out}}{\sqrt{R_{\rm out}^2 - r^2 + 0.02}} E_1$$

or

$$\sqrt{2\pi R_{\rm out}/H}\, E_1 ,$$

where the small constant 0.02 and the second expression keep the modeled emission from diverging at values of r approaching $R_{\rm out}$. The CM profile was computed out to $r = 1.19\ R_{\rm U}$ in the plane of the sky, where the emission was negligible.

The modeled CM intensity distribution was then convolved with the instrumental imaging PSF. Figure 22 shows the unconvolved modeled emission intensity along the slit normalized to unit area and the result of its convolution with the imaging PSF for both the average of the 1995 CGS4 observations and the 1993 CSHELL observations. For the CGS4, the PSF was estimated to be a radius of 1 diode (1.″23) for a spot enclosing 80% of the energy from a point source. For CSHELL, the corresponding imaging PSF was assumed to be 0.58 diode (1 diode = 0.″28); i.e., small compared to the seeing but enough to smooth the numerical emission discontinuity at the limbs. Because CSHELL has a smaller projected diode size, the spatial resolution is greater than for CGS4 but the S/N per diode is correspondingly less. For this reason, the plots below of the

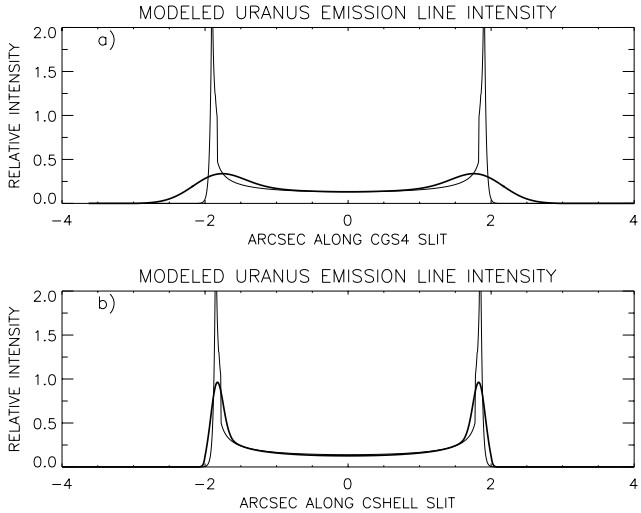

FIG. 22.—Thick-shell models of Uranus's H_2 emission (*light line*) normalized to unit area and their convolution (*bold line*) with the instrumental PSF for (*a*) CGS4 in 1995 June and (*b*) CSHELL in 1993 May. CSHELL's PSF is estimated. These models were further convolved with the diode width, a Gaussian seeing profile, and a drift hat function before comparison with the observations. Uranus's projected polar diameter was 3″ and 3.″60, respectively.

observed CSHELL emission show both the unsmoothed profile (*light lines*) and the profile boxcar smoothed by three diodes (*heavy lines*). The plotted profiles observed with CGS4 (*heavy lines*) are unsmoothed.

The emission profile was then convolved with a Gaussian seeing profile, with the seeing left as a fitted parameter determined by fitting. Since Uranus's disk is not large compared to the seeing, a two-dimensional convolution was required. However, we neglected the effect of the width of the slit on the observed central meridian profile and evaluated the two-dimensional convolution only along the bisector of the slit. We also neglected the planet's equatorial bulging. Integrating the convolution integral in polar coordinates centered on the planet's center, the angular integral separates out to a circular integral over the offset Gaussian. This yields the zeroth-order Bessel function of an imaginary argument $I_0(ry/\sigma^2)$, where r is the radius of the integration ring, y is the offset of the Gaussian, and σ is the Gaussian dispersion. The integral over r of the emission $f(r)$ yields the seeing-blurred image along the slit y:

$$F(y) = \frac{1}{\sigma^2}\int_0^\infty f(r)\,\exp\left(-\frac{r^2+y^2}{2\sigma^2}\right) I_0\left(\frac{ry}{\sigma^2}\right) dr\ .$$

The resulting profile was then convolved with a hat function of width representing the drift during the observation. For CSHELL, the drift was assumed to be small relative to other sources of broadening and so was set to 0.″15. For CGS4, the drift was taken to be 0.″5, the amplitude of the 1 Hz UKIRT tracking oscillation as derived from the stellar profiles: We estimated this amplitude by fitting a Gaussian seeing profile convolved with the CGS4 imaging PSF, the 1.″23 diode width, and a drift hat function to the stellar profiles measured along the slit for each night observed in 1995. The logged seeing was ~0.″8–1.″2, but the measured FWHM for each night was 1.″53, 1.″61, 1.″61, and 1.″41, respectively, leading to approximately a 0.″5 oscillation amplitude.

Finally, the profile was convolved with the diode width. Because of the large diodes of CGS4 (1.″23), it was necessary to adjust the phasing of the diodes along the CM in the synthetic profile in order to permit close comparison with the CGS4 observations. The fitting was then done by adjusting the intensity scale of the modeled profile and varying the seeing.

REFERENCES

Allen, C. W. 1976, Astrophysical Quantities (3d ed.; London: Athlone)
Atreya, S. K., Kerr, R. B., Upson, W. L., II, Festou, M. C., Donahue, T. M., Barker, E. S., Cochran, W. D., & Bertaux, J. L. 1982, ApJ, 262, 377
Baines, K. H., Yanamandra-Fisher, P. A., Lebofsky, L. A., Momary, T. W., Golisch, W., Kaminski, C., & Wild, W. J. 1998, Icarus, 132, 266
Ballester, G. E., Miller, S., Tennyson, J., Trafton, L. M., & Geballe, T. R. 1994, Icarus, 107, 189
Ben Jaffel, L., Prange, R., Emerich, C., Vidal-Madjar, A. & McConnell, J. C. 1991, J. Geophys. Res., 96, 9781
Birnbaum, A., & Poll, J. D. 1969, J. Atmos. Sci., 26, 943
Black, H. H., van Dishoeck, E. F., Willner, S. P., & Woods, R. C. 1990, ApJ, 358, 459
Broadfoot, A. L., et al. 1986, Science, 233, 74
Cravens, T. E. 1987, J. Geophys. Res., 92, 11083
Dabrowski, I. 1984, Canadian J. Phys., 62, 1639
Dinelli, B. M., Miller, S., & Tennyson, J. 1992a, J. Mol. Spectrosc., 153, 718
———. 1992b, J. Mol. Spectrosc. 156, 243
Drossart, P., et al. 1989, Nature, 340, 539
Emerich, E., Ben Jaffel, L., & Prange, R. 1993, Planet Space Sci., 41, 363
Geballe, T. R., Jagod, M.-F., & Oka, T. 1993, ApJ, 408, L109
Geballe, T. R., & Oka, T. 1989, ApJ, 342, 855
Gezari, D. Y., Schmitz, M., Pitts, P. S., & Mead, J. M. 1993, Catalog of Infrared Observations, NASA Reference Publication 1294 (3d ed.; Washington, DC: NASA)
Herbert, F., & Sandel, B. R. 1994, J. Geophys. Res., 99, 4143
Herbert, F., Sandel, B. R., Yelle, R. V., Holberg, J. B., Broadfoot, A. L., Shemansky, D. E., Atreya, S. K., & Romani, P. N. 1987, J. Geophys. Res., 92, 15,093
Jennings, D. E., & Brault, J. W. 1983, J. Mol. Spectros., 102, 265
Karkoschka, E. 1998, Science, 280, 570
Kim, S. J., Drossart, P., Caldwell, J., & Mailllard, J. P. 1990, Icarus, 84, 54
Kim, Y. H., Fox, J. L., & Porter, H. S. 1992, J. Geophys. Res., 97, 603
Koorneef, J. 1983, A&AS, 51, 489
Kurucz, R. L. 1970, ATLAS: A Computer Program for Calculating Model Stellar Atmospheres (SAO Special Rept. 309) (Cambridge: SAO)
Lam, H. A., Achilleos, N., Miller, S., Tennyson, J., Trafton, L. M., Geballe, T. R., & Ballester, G. E. 1997a, Icarus, 127, 379
Lam, H. A., Miller, S., Joseph, R. D., Geballe, T. R., Trafton, L. M., Tennyson, J., & Ballester, G. E. 1997b, ApJ, 474, 73L
Miller, S., Achilleos, N., Ballester, G. E., Lam, H. A., Tennyson, J., Geballe, T. R., & Trafton, L. M. 1997, Icarus, 130, 57
Miller, S., Joseph, R. D., & Tennyson, J. 1990, ApJ, 360, L55

Mohler, O. C., Pierce, A. K., McMath, R. R., & Goldberg, L. 1950, Photometric Atlas of the Near Infrared Solar Spectrum (Ann Arbor: Univ. Michigan Press)
Oka, T. 1981, Philos. Trans. R. Soc. Lond., A303, 543
Oka, T., & Geballe, T. R. 1990, ApJ., 351, L53
Rothman, L. S., et al. 1996, The HITRAN Molecular Spectroscopic Database and HAWKS (HITRAN Atmospheric Workstation) (Hanscom Air Force Base, MA: USAF Phillips Laboratory)
Schild, H., Miller, S., & Tennyson, J. 1997, A&A, 318, 608
Stallard, T., Miller, S., Ballester, G. E., Rego, D., Joseph, R. D., Trafton, L. M. 1999, ApJ, 521, L149
Stevens, M. H., Strobel, D. F., & Herbert, F. 1993, Icarus, 100, 45
Trafton, L. M. 1976, ApJ, 207, 1007
———. 1987, Icarus, 70, 13
Trafton, L. M., Carr, J., Lester, D. F., & Harvey, P. 1987, Icarus, 74, 351
———. 1989a, in Time Variable Phenomena in the Jovian System, ed. M. J. Belton, R. A. West, & J. Rahe (NASA SP-494), 229
Trafton, L. M., Geballe, T. R., Miller, S., Tennyson, J., & Ballester, G. E. 1993, ApJ 405, 761
Trafton, L. M., Lester, D. F., & Thompson, K. L. 1989b, ApJ, 343, L73
Turner, J., Kirby-Docken, K., & Dalgarno, A. 1977, ApJS, 35, 281
Waite, H. J., Jr., Cravens, T. E., Kozyra, J., Nagy, Atreya, S. K., & Chen, R. H. 1983, J. Geophys. Res., 88, 6143